

**PREDICTION OF DELAMINATION IN FLEXIBLE SOLAR CELLS:
EFFECT OF CRITICAL ENERGY RELEASE RATE IN COPPER INDIUM
GALLIUM DISELENIDE (CIGS) SOLAR CELL**

by

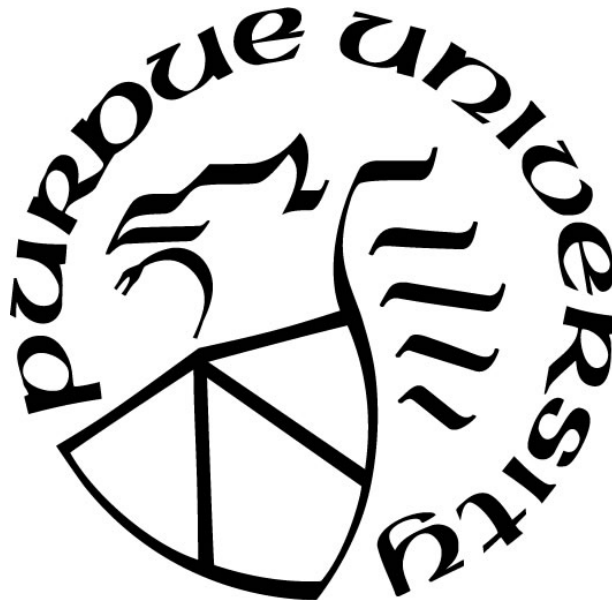
Roger Eduardo Ona Ona

A Thesis

Submitted to the Faculty of Purdue University

In Partial Fulfillment of the Requirements for the degree of

Master of Science in Mechanical Engineering



Department of Mechanical and Civil Engineering

Hammond, Indiana

December 2021

THE PURDUE UNIVERSITY GRADUATE SCHOOL
STATEMENT OF COMMITTEE APPROVAL

Dr. Hansung Kim, Chair

Department of Mechanical and Civil Engineering

Dr. Nesrin Ozalp

Department of Mechanical and Civil Engineering

Dr. Xiuling Wang

Department of Mechanical and Civil Engineering

Dr. Harvey Abramowitz

Department of Mechanical and Civil Engineering

Approved by:

Dr. Xiuling Wang

Dedicated to my family

ACKNOWLEDGMENTS

I would want to express my gratitude to Dr. Hansung Kim of his help and advice throughout my master's degree program. His advice and unwavering support have been crucial throughout the study process. I would like to express my sincere gratitude to the other members of my committee, Dr. Xiuling Wang, Dr. Harvey Abramowitz and Dr. Nesrin Ozalp for volunteering their time to serve on my committee. I also extend my thanks to the department of Mechanical Engineering for providing me the opportunity to work as teaching assistant. During my time at Purdue University Northwest, this enriching opportunity has allowed me to improve both personally and professionally.

Finally, I would like to express my gratitude to my family for their unwavering support and encouragement. I would not have done it without their unwavering and unconditional love and support, despite our geographical distance. I cannot describe how grateful I am to them in words. Gracias!

TABLE OF CONTENTS

LIST OF TABLES	7
LIST OF FIGURES	8
ABSTRACT	10
1. INTRODUCTION	11
1.1 Background	11
1.2 Flexible solar cells.	13
1.3 Delamination using different techniques	14
1.4 Outline of the thesis	15
2. FUNDAMENTAL THEORIES.....	16
2.1 Introduction to fracture mechanics	16
2.2 Literature on cohesive model.....	19
2.3 J- integral concept	20
2.4 Energy balance during a crack growth using peeling test.....	22
2.5 Literature review	26
2.6 Objectives	28
3. EXPERIMENTAL PROCEDURE.....	29
3.1 Overview.....	29
3.2 Orientation angle for the experiment	30
3.3 Sample material	32
3.4 Procedure for measuring the mechanical properties of the peel arm.....	36
3.5 Procedure for measuring the properties of the bottom layer.....	38
3.6 Procedure for the peeling test	39
4. SIMULATION PROCEDURE.....	43
4.1 Finite element simulations	43
4.2 Peeling simulation using COMSOL software.....	43
4.2.1 J-integral using the COMSOL software	44
4.2.2 Three-dimensional (3-D) model of the sample test	45
4.2.3 The cohesive zone model simulation in the COMSOL software	46
4.2.4 Mesh generation.....	47

5. RESULTS AND DISCUSSION.....	49
5.1 Peeling arm data.....	49
5.2 Obtaining parameters for the bottom layer	50
5.3 Peeling test data	51
5.4 Energy release rate	55
5.5 Results in COMSOL.....	56
5.5.1 J-integral results	56
5.5.2 Cohesive model results	58
6. CONCLUSION AND FUTURE WORK	62
6.1 Conclusion	62
6.2 Future work	63
REFERENCES	65
APPENDIX A. MATERIAL COMPOSITION FOR CIGS LAYER.....	72
APPENDIX B. PEEL ARM PROPERTIES	75
APPENDIX C. BOTTOM LAYER PROPERTIES	79
APPENDIX D. PEELING TEST RESULTS	83

LIST OF TABLES

Table 1. Typical Composition of a CIGS PV Cell [7].	14
Table 2. Mechanical and physical properties of materials used in this study.	43
Table 3. Mechanical properties for the peeling arm.	50
Table 4. Information for the Bottom Layer (SS)	51
Table 5. Peel Results for flexible protection and ZnO interface for multiple angle configurations	53
Table 6. Peel Results for Mo and SS interface for multiple angle configurations.	54
Table 7. Material properties used in the energy calculation	55

LIST OF FIGURES

Figure 1.1. Sketch of a photovoltaic (PV) effect in a solar cell [2].	12
Figure 2.1. Potential energy and force as a function of atomic separation. X_0 represents the equilibrium separation of atoms where the attractive and repelling forces are balanced [18].	18
Figure 2.2. Simple representation of a traction -separation curve.	20
Figure 2.3. Schematic comparison of the stress strain behavior of elastic-plastic and nonlinear elastic materials [18].	20
Figure 2.4. The path independency in J-integral [34].	21
Figure 2.5. Schematic of the thin film as it is peeled.	22
Figure 2.6. Presentation for the stress vs strain curves of a CIGS peel arm.	24
Figure 2.7. Bending and unbending process of the peel arm during single peeling [36].	24
Figure 2.8. Bending and unbending deformation in the peel arm during peeling [35].	25
Figure 2.9. Deformation of the peeling arm.	26
Figure 2.10. A cohesive zone ahead of a crack [48].	27
Figure 2.11. J-integral applied in two different paths [48].	28
Figure 3.1. Flexible solar cell. (a) Hanergy SP-08 flexible CIGS. (b) Sample test for all experiments.	30
Figure 3.2. MTS Fundamental 90-degrees peel fixture machine.	31
Figure 3.3. Custom plates for 45, 60, and 90-degrees.	31
Figure 3.4 Scanning electron microscope (SEM) images of CIGS solar cells showing the cross-sections of the multilayer film.	32
Figure 3.5. High resolution scanning electron microscope image (SEM) of a CIGS solar cell showing Mo/SS interface.	33
Figure 3.6. Layer composition of a CIGS solar cell [58].	34
Figure 3.7. Specimen after peeling test. (a) Peel arm(presence of Mo), (b) bottom layer(presence of Mo and other materials in the film).	35
Figure 3.8. Uniaxial tensile test using a contact extensometer.	36
Figure 3.9. Uniaxial tensile test without contact extensometer.	37
Figure 3.10. Tensile test for the peeling arm.	38
Figure 3.11. Bottom layer with protection.	39

Figure 3.12. Fixed arm peel fixture with linear bearing system showing a 90-degree peel angle.	39
Figure 3.13. Force vs displacement for 90-degree peeling test.	40
Figure 3.14. Average peel force vs displacement in 90-degree peeling test.....	41
Figure 4.1. Contour around the crack tip used in the definition of J-integral.....	44
Figure 4.2. Configuration for 90-degree peeling test.....	45
Figure 4.3. Traction-separation law used for the estimation both normal strength and penalty stiffness.	47
Figure 4.4. Contact pair: a) Source boundaries. b) Destination boundaries.	47
Figure 4.5. Mesh generation for a realistic peel test in 90-degree.	48
Figure 5.1. Important Parameters in the Peel Arm. (a) Without extensometer, (b) Using a contact extensometer.	49
Figure 5.2. Force vs displacement for 90-degree peeling test.	52
Figure 5.3. Force vs displacement. (a) 45-degree peeling test. (b) 60-degree peeling test.....	52
Figure 5.4. Peeling settings. (a) Initial crack, (b) 45-degree, (c) 60-degree, and (d) 90-degree...	53
Figure 5.5. Average peeling force vs peel angle.....	54
Figure 5.6. Normal stress distribution in X direction around the crack tip for 90-degree.....	57
Figure 5.7. Displacement vs J-integral for 90-degree peeling test.	57
Figure 5.8. Displacement vs J-integral. (a) 45-degree test. (b) 60-degree peeling test.	58
Figure 5.9. Equivalent stress (Pa) distributions for 90 degrees.	58
Figure 5.10. Progressive interface delamination.....	59
Figure 5.11. Experimental and numerical 90-degree peeling test.	60
Figure 5.12. Improved results for the 90-degree peeling test.	60
Figure 5.13. Progressive increment in energy	61

ABSTRACT

Solar cells are a multilayer structure, which are constantly exposed to adverse weather conditions and UV rays. Interfacial cracks and extreme external conditions can reduce the solar cell's performance and durability. The interface in a multilayer Copper Indium Gallium Diselenide (CIGS) solar cell was studied applying the principles of fracture mechanics to a fixed-arm-peel test. The energy release rate (G_a), which is the energy required for the interfacial delamination, was obtained with this process. In this case, the interface between the molybdenum (Mo) and stainless steel (SS) of the multilayer CIGS solar cell were selected for the analysis. Experiments and finite element (FE) modeling simulations were used to investigate the interfacial delamination, so the prediction of delamination can be achieved by using the cohesive model.

The experiment consisted of obtaining the material properties of the solar cell specimen and the energy required to start the delamination. A uniaxial tensile test was used to obtain the material properties of the solar cell, such as young's modulus and yield strength. A fixed-arm-peel test was used to obtain the peeling force for different peeling angles. The material properties and the peeling force were processed in several non-linear equations, so the energy release rate (G_a) was obtained.

Fracture mechanics was simulated in a finite element software, and two and three-dimensional simulations for J-integral and cohesive models respectively were carried out to compare the experimental with the numerical peeling force. J-integral simulation and peeling test results were used to estimate a critical separation (δ_m) of 0.5 mm. This value was used to calculate the normal strength of $8.74 \times 10^5 \text{ N/m}^2$, and the penalty stiffness could be estimated. These three parameters were used in the bilinear traction-separation law for the cohesive model in a 90-degree configuration. The accuracy of the model was compared by fitting the experimental and numerical peeling force, which had a difference of 0.08 %. It is demonstrated that the peeling process for 90-degree could be replicated in COMSOL® software for a CIGS solar cell.

1. INTRODUCTION

1.1 Background

Solar energy possesses immense potential as a safe and efficient energy source. Over the last few decades, it has been used as an alternative source of energy, which can provide light and heat. Solar energy is increasing in competitiveness against other technologies because it is a free and virtually endless source of energy. It is paramount that we avoid any harmful dependency on the "dirty" forms of energy we use, such as coal or oil, which produce CO₂ emissions and contribute to the greenhouse effect. Solar energy is a form of "clean" energy that is able to power multiple facilities without the risk of environmental pollution. All devices that convert solar energy into electricity are considered semiconductors through electrical conductivity, which is based upon movable electrons [1]. The absorption of the solar spectrum depends on the material properties of these semiconductors and a p-n junction.

A solar cell can be best classified as a semiconductor diode with special characteristics. These characteristics make it possible to obtain and use photonic energy transmitted by radiant light from the sun to generate electrical energy. The material properties in the semiconductors implemented in a typical solar cell structure provides a better absorption of the solar spectrum. Figure 1.1 shows a conventional solar cell structure. This figure and the information described in Sabu et al. [2] are used to explain the conversion of solar energy into electrical energy. In this process, the sunlight shines in the top surface of a solar cell. Light is absorbed in the cell and it creates electron-hole pairs. Then, charge carriers (either electrons or holes) move under the competing effect of two driving forces. One of the forces is the diffusion, which is the driving force in the p and n neutral regions. The second force is the drift, which controls the movement of charge carriers in the depletion region. The p-n junction at the interface between the n- and p-side behaves as a membrane. This membrane repels electrons in the n-side and holes in the p-side. Finally, electrons and holes are separately collected and injected. All this process allows solar energy to power any external circuit [2].

The process of collecting energy from the sun and converting it into electrical energy will help humanity cover the energy demand that is progressively increasing. Using solar technology, people can generate their own electricity, and the solar industry is constantly improving this

technology. The solar electricity cost has been reduced worldwide, and when this technology is compared with others, it is demonstrated that it requires less infrastructure. It is more accessible to areas where conventional electricity is not an easy option, and recent innovations have opened up many options with different features such as flexibility, different custom shapes, and transparency. The weight, which was an issue in early design stages, was drastically reduced.

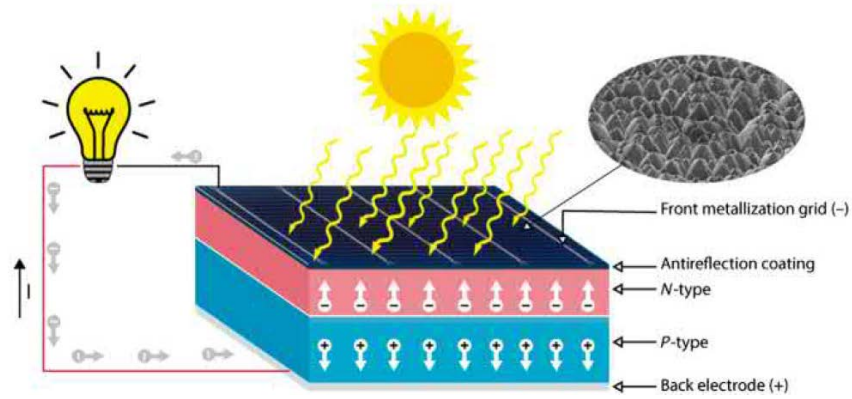


Figure 1.1. Sketch of a photovoltaic (PV) effect in a solar cell [2].

Solar cells were made of heavy glass sheets and metal frames, which were replaced by improving or completely eliminating them. The light weight generated positive results in terms of cost, because it reduces the transport and deployment values. These new characteristics helped manufacturing companies to provide different types of solar cells, which can be used according to needs and preferences of their users. The improvement in solar cells are related to the solar range, cost, protection, durability, and efficiency. External factors such as transportation, inappropriate handling during installation, environmental condition, brittle behavior of the material, etcetera, can create or propagate fractures in the solar cell material which are directly related to a decrease in performance.

Predicting solar cell fracture is a crucial problem for both producers and users, since it ensures structural integrity and satisfactory performance during service. Normally, this service has performance warranties of 20-25 years, which is unique in electrical equipment [3]. A single type of solar cell, which was Copper Indium Gallium Diselenide (CIGS) Solar Cell, was considered from all different types (further explained in the next section) in this study to understand the delamination process between two layers from its multilayer composition. The CIGS solar cell

is generally made out of five different layers, while the delamination will be evaluated in its interface using fracture mechanics and peeling test protocols.

Therefore, modeling the fracture propagation (delamination between two layers) requires the understanding of some principles of fracture mechanics as well as different peeling test protocols. The information collected will be implemented in a finite element (FE) software, and the result can be used as reference for future projects. There are hundreds of types of solar cells, so the specific solar cell used in this project can provide a standard procedure which can be adapted to other types of solar cells.

1.2 Flexible solar cells.

Most of the solar cell market is based on crystalline silicon (c-Si) solar cells owing a high efficiency of 26.7% [4]. Production cost is a major concern, since Si substrates, installation and transportation play an important role in the total cost of this system [4]. The CIGS-based solar cell, which is the principal material in this analysis, has shown a low cost, easy integration and most importantly, a remarkable efficiency [5] [6]. The efficiency of this second-generation solar cell goes around 23.4%, compared to 22.1% for CdTe and 26.1% for crystalline silicon-based PV cells [7]. A CIGS cell has a similar structure to all other semiconductor-based PV cells (Table 1) with the exception of the energy bandgap. In this case, the energy bandgap can be adjusted to values between 1 and 2.4 eV by changing the ratios of the CIGS elements (copper, indium, gallium, selenium) and the absorption of light can be maximized [8]. This solar cell has a positive environmental impact compared with CdTe PV cells, which use a layer containing cadmium, and rare earth elements such as tellurium. It still uses a layer containing cadmium, but it is much thinner than the p-type CdTe layer in CdTe PV cells [7]. An extra benefit of CIGS films is that they are stable with increasing temperature (unlike silicon-based solar cells). The low weight, customizable shape and flexibility provides more advantages over other flexible PV cells [7]. Different vacuum techniques have been developed for the production of CIGS solar cells. Mufti et al. [9] includes a review of different techniques with their pros and cons that can be utilized to fabricate CIGS-based solar cells. Among them, co-evaporation physical vapor deposition (PVD), pulsed laser deposition (PLD), chemical vapor deposition (CVD), metalorganic chemical vapor deposition (MOCVD), electron beam deposition (EBD), molecular beam epitaxy (MBE), and sputtering are regarded as the finest vacuum solutions for industrial growth, even though CIGS solar cells still have some

limitations. Due to the intricacy of the production processes and the expense of the production lines, CIGS volume production is one of the limitations [10].

One way to reduce the production cost of CIGS solar cells is to replace the conventional substrates (soda lime glass (SLG)) with a low-cost flexible substrate such as stainless steel, polyamide, and metal sheet. CIGS solar cells on soda lime glass substrates has a record efficiency of 23.4% [7] compared with flexible substrates such as stainless steel foil (19.4%) and polyamide (20.4%) [11]. The cost can be reduced, but the efficiency is compromised. Flexible light-weight solar cells are gaining considerable attention because of the easy-to-install feature on any portable device. Automobiles, houses' roofs, and practically any surface can be integrated by flexible solar cells. The photovoltaic market is constantly improving solar cell technology, and soon we will be able to have a complete transition from fossil fuels-based technology to renewable energies.

Table 1. Typical Composition of a CIGS PV Cell [7].

Layer	Material	Function
Window layer	Aluminum zinc oxide (Al,ZnO)	Transparent; reduces recombination and current loss
Transparent conducting electrode	Zinc oxide (ZnO)	Antireflective; Collects electrons
n-type layer	n-type cadmium sulfide (CdS)	Transports electrons
p-type layer Back-side contact	p-type copper indium gallium selenide (CIGS) Molybdenum (Mo)	Transports holes Collects holes; reflects light back into CIGS
Substrate	Soda lime glass, metal foil, or plastic	Increases open circuit voltage of cell; provides structural stability

1.3 Delamination using different techniques

Delamination in composite materials is a major concern in any type of industry, and there are various theoretical models used for describing this type of failure. Principles of fracture mechanics and peeling test protocols are covered in the next chapter, and it is important to mention some important theoretical concepts such as J-integral and cohesive zone. The J-integral is determined by specifying a closed path around a crack, so it is possible to characterize of the energy intensity of elastic-plastic crack-tip fields [12]. The cohesive zone concept describes cohesive forces required to initiate and propagate the delamination growth using a traction-

separation curve. Using these concepts and peeling test protocols, the energy required to initiate the peeling process is obtained. This is used to compare the experimental and mathematical peel force using COMSOL. Once the results are obtained, these can be used to predict the delamination in different types of solar cells by adapting the numerical model.

1.4 Outline of the thesis

This thesis is divided into six chapters, including this introductory chapter.

Chapter 2 condenses fundamental theories. It explains the theory behind the interfacial delamination using fracture mechanics and the peeling test. For fracture mechanics, J-integral and cohesive zone are explained, and these concepts are used to understand and implement the energy involved in the interfacial delamination, known as “energy release rate” in the numerical analysis. The peeling test, on the other hand, is used to describe the mechanics of peeling, so the energy release rate can be obtained and compared with the numerical analyses.

Chapter 3 covers the experimental procedure in the peeling test and a uniaxial tensile test for two selected layers from a CIGS solar cell. The 90-degree peeling test is carried out in order to obtain the energy required to propagate an interfacial delamination. The uniaxial tensile test for two-selected layers are implemented to obtain the material properties of the solar cell, which are used in the numerical analysis.

Chapter 4 describes the parameters and procedures in the numerical analyses using COMSOL Multiphysics. The geometry was carefully designed in order to simulate a realistic situation for the 90-degree peeling test, so the numerical results can be validated with the experimental data.

Chapter 5 summarizes the experimental and simulation results by investigating the critical energy release rate using the 90-degree peel test. This part also discusses the validity of the theoretical model used in the simulation.

Chapter 6 condenses the main conclusions of the thesis and discusses possible research areas. The 90-degree test was used in a GICS solar cell with a numerical simulation, but it can be extended to different peel angles.

2. FUNDAMENTAL THEORIES

2.1 Introduction to fracture mechanics

Fracture mechanics is the study of the processes in the formation and propagation of cracks subjected to a different condition, such as mechanical, thermal, and/or electromagnetic stress. These cracks are created when the atomic bonds that hold atoms together are broken due to sufficient stress and work. The principle of fracture mechanics was developed by Irwin [13] using the mathematical analysis of Inglis [14], Griffith [15], and Westergaard [16]. This principle deals with the complex fracture process due to the nucleation and growth of cracks, which depends on several factors. The formation of cracks is highly dependent on the microstructure of a crystalline or amorphous solid, applied loading, and environmental conditions [17]. On a microscopic level, materials present some imperfections within the crystalline structure, which can act as a fracture origin in extreme conditions.

Fracture mechanics requires an understanding of the stress near fracture tips as well as the energy conditions that cause fracture propagation in elastic, plastic, or visco-plastic materials [17]. A brittle fracture, for instance, is a low-energy process that reaches its failure without significant plastic deformation, or any warning since the crack velocity is normally high. On the other hand, a ductile fracture requires a large plastic deformation before a crack can occur, and a large amount of energy dissipation. These requirements make a slow crack growth compared with brittle materials [17]. Linear-elastic fracture mechanics (LEFM) and elastic-plastic fracture mechanics (EPFM) are two types of fracture mechanics. For brittle elastic materials or when the applied force is low enough, LEFM produces great results. It uses the strain energy release rate G , or the stress intensity factor K , as a fracture criterion. However, in the presence of plastic deformation characterized in ductile materials, LEFM must be replaced by EPFM, which measures the fracture toughness using the distance between the crack faces at the deformed tip.

The bond energy required to increase the separation distance between atoms in fracture mechanics is given by [18]:

$$E_b = \int_{x_0}^{\infty} P dx \quad (1)$$

The equilibrium spacing between atoms is represented by x_0 and P is the applied force (see Figure 2.1). Assuming a simple force-displacement law with a half period, it is possible to estimate the cohesive strength. This condition modifies the formula to:

$$P = P_c \sin\left(\frac{\pi x}{\lambda}\right) \quad (2)$$

Where P_c is the magnitude of the force applied, and λ represents the distance where the force-displacement relationship is linear:

$$P = P_c \left(\frac{\pi x}{\lambda}\right) \quad (3)$$

and the bond stiffness is given by:

$$k = P_c \left(\frac{\pi}{\lambda}\right) \quad (4)$$

Multiplying both sides of this equation by the equilibrium spacing between atoms (x_0) and the number of bonds (n) per unit area (A). Rearranging the formula, Young's modulus (E) and cohesive stress can be given by:

$$\left(\frac{n}{A(=1)}\right)(x_0)k = P_c \left(\frac{n}{A(=1)}\right)(x_0) \left(\frac{\pi}{\lambda}\right) \quad (5)$$

Where:

$$\delta = \frac{PL}{EA} \rightarrow P = \frac{EA}{L} \delta, \quad k = \frac{EA}{L} \rightarrow E = \frac{kL}{A} \quad (6)$$

$$E = (\sigma_c) \left(\frac{\pi x_0}{\lambda}\right) \quad (6)$$

$$\sigma_c = \frac{E \lambda}{\pi x_0} \quad (7)$$

When λ is assumed to be approximately equal to the atomic spacing (x_0), σ_c becomes:

$$\sigma_c \approx \frac{E}{\pi} \quad (8)$$

The fracture creates two surfaces, so the surface energy per unit area, γ_s , is equal to one-half of the fracture energy given by:

$$\gamma_s = \frac{1}{2} \int_0^\lambda \sigma_c \sin\left(\frac{\pi x}{\lambda}\right) dx = \sigma_c \frac{\lambda}{\pi} \quad (9)$$

Where:

$$\sigma_c \sin\left(\frac{\pi x}{\lambda}\right) \rightarrow \text{force per unit area}$$

$dx \rightarrow \text{distance}$

Using Equation (7) and Equation (9) the cohesive stress in terms of surface energy is given by:

$$\sigma_c = \frac{E \lambda}{\pi x_0} \rightarrow \lambda = \frac{\sigma_c \pi x_0}{E} \quad (7)$$

$$\gamma_s = \sigma_c \frac{\lambda}{\pi} = \sigma_c \frac{1}{\pi} \left(\frac{\sigma_c \pi x_0}{E} \right) = \sigma_c^2 \frac{x_0}{E} \quad (9)$$

$$\sigma_c \rightarrow \sqrt{\frac{E \gamma_s}{x_0}} \quad (10)$$

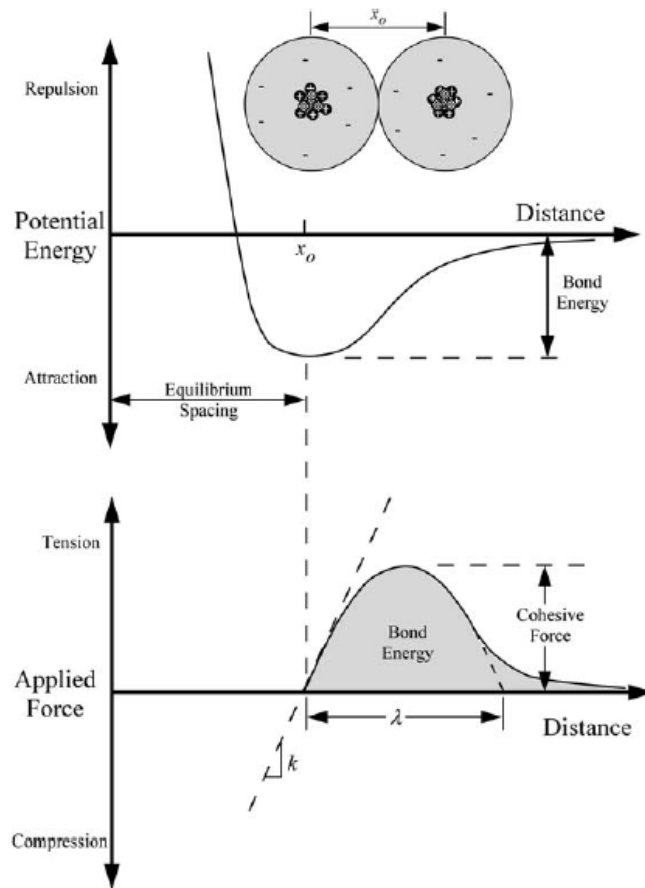


Figure 2.1. Potential energy and force as a function of atomic separation. x_0 represents the equilibrium separation of atoms where the attractive and repelling forces are balanced [18].

2.2 Literature on cohesive model.

The Cohesive Model (CM) started as early as 1960 when Dugdale solved the problem of unrealistic continuum mechanics stress singularity at the crack tip. He introduced a strip—yield model where he assumes a plastic zone [19](cohesive force) which prevents the crack extension. Under crack opening Mode I load, the length of the plastic zone ahead of a crack is determined when the applied stress reaches the yield strength. Later, Barenblatt [20] developed the fundamental idea for the CM for the decohesion of atomic lattices using traction–separation law (TSL) later known as cohesive law. In Barenblatt’s model, the traction is expressed as a function of the distance from the crack tip, but actual models define the traction as functions of the separation within the cohesive zone [20]. This knowledge was later used by Hillerborg et al. to describe the damage behavior of concrete, and Petersson developed a so-called fictitious crack Model1 to explain how it affects the crack propagation and the fracture process for plain concrete [21].

Further developments in this area has attracted much attention because it was the first application of the CM, see the work of the research groups of Elices [22] , Planas [23], Bazant [24], and Carpinteri [25] who provide a compressive overview of the CM in concrete structures. In brittle materials, the maximum cohesive strength is reached at the beginning of the crack propagation without showing any soft strength increment. For material such as metal and their alloys, fundamental work has been performed by Needleman [26], Tvergaard and Hutchinson [27] [28], Lin [29] and Cornec [30]. These concepts provide by different authors demonstrated the CM’s ability to address a wide range of materials and fracture mechanisms.

To model the separation process using the cohesive model, it is required two parameters in order to formulate the cohesive model as a traction-separation law. This law relates the traction (τ) and separation (δ) which can be represented as a linear or bilinear function. A representation of a bilinear traction-separation law is shown in Figure 2.2. The traction (τ) is the stress required to separate the adjacent surface. The separation (δ) is the relative displacement between surfaces or the separation within the cohesive zone. Under external loading, τ_{max} reaches its maximum value corresponding to δ_c . After this point, the crack is initiated and the material starts a process of irreversible damage where the cohesive traction is zero at a critical separation value (δ_m) [31]. The area under traction-separation curve is defined as fracture toughness of the material or interfacial fracture toughness of the interface [32].

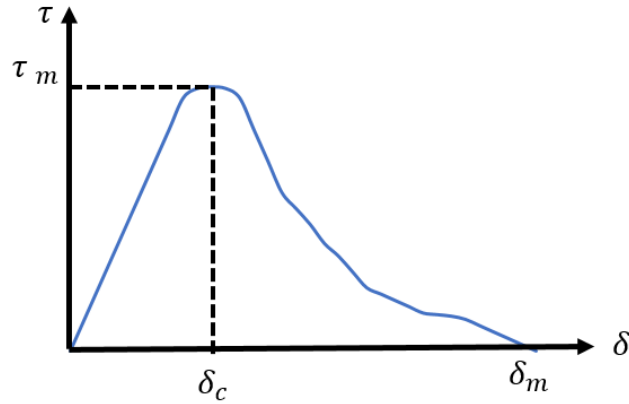


Figure 2.2. Simple representation of a traction -separation curve.

2.3 J- integral concept

Linear and nonlinear elastic fracture mechanics are used to explain practical problems in engineering mechanics. In linear elastic fracture, the material is assumed to be isotropic and linear elastic. Under an external load, the stress field near the crack tip can be calculated using theory of elasticity [18]. If the material has a large presence of plastic deformation at the crack tip, the theory of elasticity is no longer valid and an alternative nonlinear fracture mechanics model is needed. Figure 2.3 illustrates how the elastic-plastic material unloads along a linear path with a slope equal to young's modulus, whereas the nonlinear elastic material unloads along the same path as when it was loaded [18].

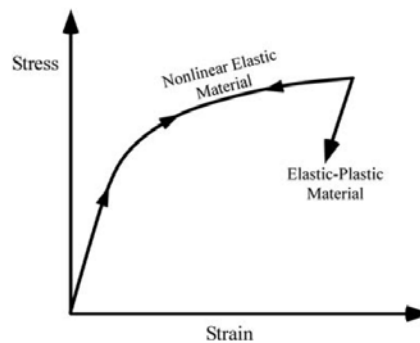


Figure 2.3. Schematic comparison of the stress strain behavior of elastic-plastic and nonlinear elastic materials [18].

Rice JR [31] in 1968 proposed a new fracture parameter to the analysis of a crack in a nonlinear material that was later known as J integral defined as:

$$J = \oint_{\Gamma} \left(w \, dy - T_i \frac{\partial u_i}{\partial x} \, ds \right) \quad (11)$$

The arbitrary curve around the tip of a crack (Γ) is presented in Figure 2.4. The integral being evaluated can be counterclockwise or clockwise, but they need to close the path around the crack.

Where

w = strain energy density

T_i = components of the traction vector

u_i = displacement vector components

ds = length increment along the contour

x and y = rectangular coordinates with the y direction taken normal to the crack line and the origin at the crack tip.

Using Rice's approach, the extension of a crack can be associated with the energy release rate in nonlinear elastic materials required for the crack propagation.

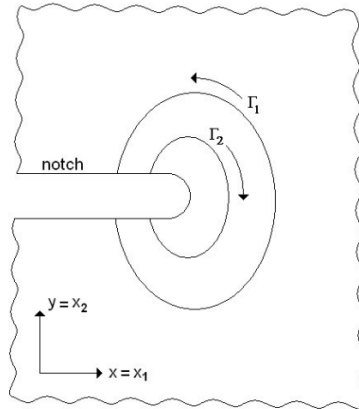


Figure 2.4. The path independency in J-integral [32].

2.4 Energy balance during a crack growth using peeling test

There are many established experimental methods described by several authors where they explain the mechanics of peeling. This description determines the adhesion strength in laminates used in different application, but the description given by [33] were used in this report. Kinloch et al. [33] describes the most relevant achievements using the mechanics of peeling and reviews basic concepts about the adhesive fracture energy. Here, the fracture energy (G_a) (material parameter) is calculated using an energy balance argument.

$$G_a = \frac{1}{b} \left(\frac{dU_{ext}}{da} - \frac{dU_s}{da} - \frac{dU_{dt}}{da} - \frac{dU_{db}}{da} \right) \quad (12)$$

Where

dU_{ext} = external work

dU_s = stored strain energy in the peel arm

dU_{dt} = energy dissipated during tensile deformation of the peel arm

U_{db} = energy dissipated during bending of the peel arm near the peel front

d_a = peel fracture length.

b = width of the specimen

From this formula, it is necessary to derivate the value of G_a that considers the tensile deformation and bending of the peel arm which dissipate energy during the process. Figure 2.5 illustrated one of the most frequently used ways for determining the failure of flexible laminates [33].

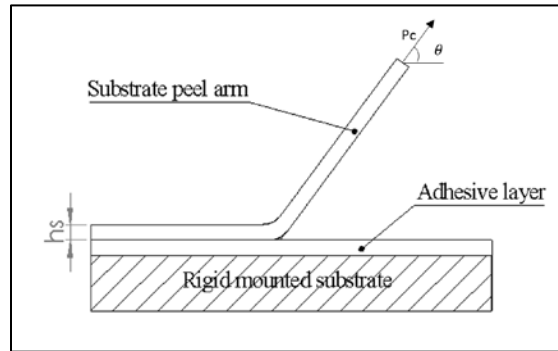


Figure 2.5. Schematic of the thin film as it is peeled.

Now considering the film being peeled in a steady-state under constant load P_c at an applied angle θ then:

$$dU_{ext} = P_c da (1 + \varepsilon_a - \cos\theta) \quad (13)$$

$$d(U_s + U_{dt}) = bh_s da \int_0^{\varepsilon_a} \sigma d\varepsilon \quad (14)$$

Where σ and ε refer to the stress versus strain behavior of the peel arm, h_s is the thickness, b width and ε_a is the tensile strain in the peeling arm.

Assuming the peeling arm has an infinite tensile stiffness ($\varepsilon_a = 0$) and zero bending stiffness (assumptions frequently made and justify by Kinloch et al.), the equation can simplify to:

$$G_a^{\infty E} = \frac{P_c}{b} (1 - \cos\theta) \quad (15)$$

Considering deformation such as stretching of the peeling arm, but assuming an only elastic bending of the peel arm, then the equation can be obtained:

$$G_a^{eb} = \frac{P_c}{b} (1 + \varepsilon_s - \cos\theta) - h_s \int_0^{\varepsilon_a} \sigma d\varepsilon \quad (16)$$

The peel arm is able to store energy in an elastic, non-work hardening material which is represented by the maximum elastic energy (per unit width per unit length).

$$G_{max}^e = \frac{\sigma_y \varepsilon_y h_s}{2} = \frac{E_s \varepsilon_y^2 h_s}{2} \quad (17)$$

Where σ_y is the yield stress, ε_y is the yield strain and E_s is the Young's modulus of the peel arm. The procedure for finding these terms will be completely explained in chapter 3, and Figure 2.6 illustrate the stress-strain relation for the peel arm using CIGS solar cell.

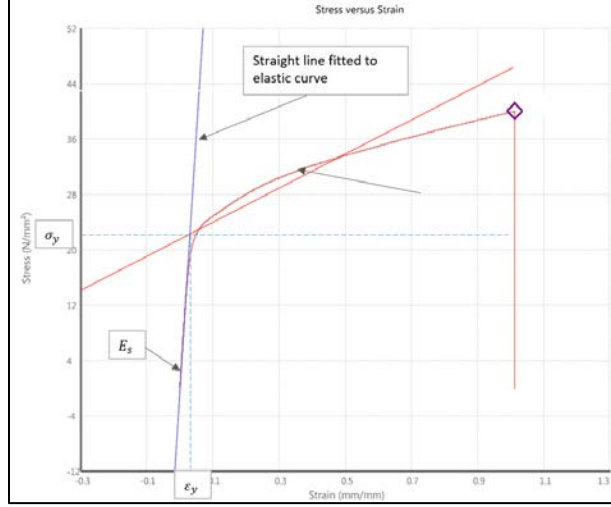


Figure 2.6. Presentation for the stress vs strain curves of a CIGS peel arm.

Considering the energy losses due to plastic or viscoelastic bending of the peeling arm near the crack, the value of G_a is given by:

$$G_a = \frac{P_c}{b} (1 + \varepsilon_s - \cos\theta) - h_s \int_0^{\varepsilon_a} \sigma d\varepsilon - G_{db} \quad (18)$$

Or

$$G_a = G_a^{eb} - G_{db} \quad (19)$$

G_{db} is the plastic work done in the bending of the peel arm. This value can become zero if elastic conditions are maintained. However, if these conditions are not applied, large displacement beam theory is required and plastic loading, elastic-plastic unloading and root rotation at the peel front must be considered. The process of bending and unbending of the peel arm during the peeling process (see Figure 2.7) can be divided in three stages for better understating about the importance of the elastic or inelastic deformation of the peel arm.

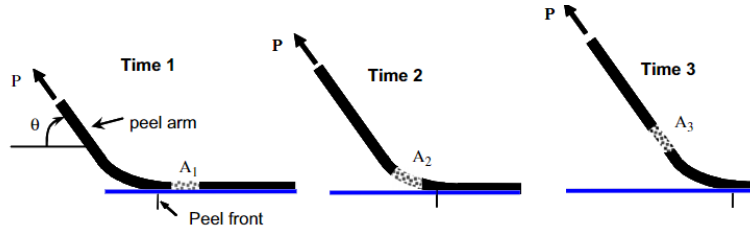


Figure 2.7. Bending and unbending process of the peel arm during single peeling [34].

During the first stage, there is a straight segment in the bonded region (A_1). In the second stage, a force is applied to the peel arm, which initializes the debonding process. The force makes the peel arm to bend (A_2) as it begins to peel upward reaching its maximum momentum(M_o) [33]. This maximum momentum has a slope of θ_o , and it is located at the crack propagation represented by “A” in Figure 2.8 and Figure 2.9 [33]. The third stage occurs when the crack is created and the peel arm is unbonded. The bending in the arm is unloaded and it is represented by “C” in Figure 2.8 and Figure 2.9 [33]. In this situation, the peel arm has a peel angle of θ degrees and it is straight again which is represented by the section A_3 in Figure 2.7. The region [COD] in Figure 2.8 is a loss of elastic energy, which is not considered in the analysis because it is not available from the debonding process [33]. On the other hand, the area [OABC] represents the total energy loss in the loading and unloading cycle in the peel arm know as G_{db} in equation 18 or equation 19.

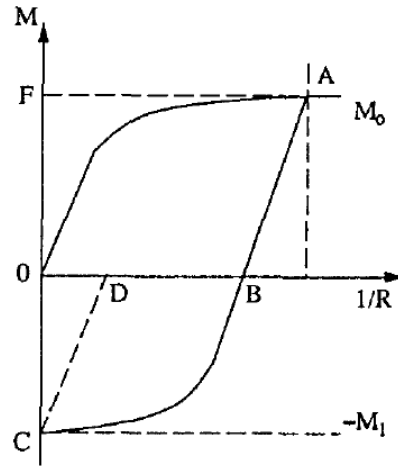


Figure 2.8. Bending and unbending deformation in the peel arm during peeling [33].

The loading and unloading of the peel arm during different stages can involve elastic-elastic, plastic -elastic or plastic-plastic deformation. The general scheme for modeling the local bending was reviewed by Kinloch et al. [33] and it is followed here. These combinations of plastic and elastic deformation in the peel arm was later related in more details in the next chapters for the specific case in CIGS films. Indeed, an analytical estimate written by the Imperial College of London called ICPeel [35] was used calculate the critical energy release rate. The ICPeel deals with some assumptions made for idealizing the peel process such as infinite tensile stiffness ($\epsilon_a = 0$) and zero bending stiffness. It uses several highly non-linear equations, which includes the

inelastic bending and unbending of the peel (energy losses) [34]. It also uses properties of the peel arm, so the fracture energy (G_a) and the plastic work done in the bending of the peel arm G_{db} are calculated. Full details are given in reference [33], where more information about the elastic-plastic behavior in flexible laminates can be found.

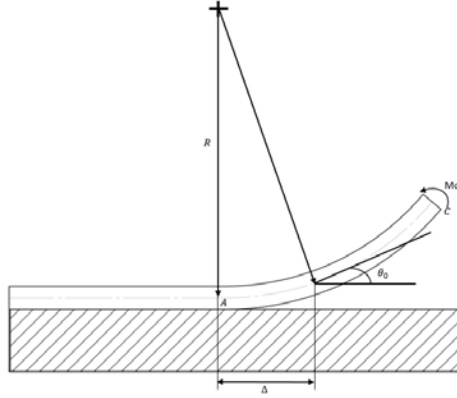


Figure 2.9. Deformation of the peeling arm.

2.5 Literature review

Unfortunately, after being manufactured, solar cells are under high risk of developing microcracks during the transportation, installation, and maintenance stage [36] and these issues are difficult to detect from simple inspection. Some authors discuss the origins, factors and power loss due to the microcracks effect. The resistance of solar cells to cracking and durability is an important aspect related both production cost and performance in solar cells. Manufacturing facility reports losses of 5-10 % due to cracking [37] and it causes degradation up to 3% per year in the first two years of operation in normal environmental conditions [38]. Other authors ([3], [39], [40], [41], [42], [43], [44], [45]) report the effect of cracks in solar cells from their detection to prediction. The conventional crack analysis is focused on imperfections in the layer, but not in the interface between them.

Understating the failure in the interface between layers can predict internal delamination (crack propagation) which is of great importance for solar cell industries, as it can lead to improve the structural integrity and performance for manufactures as well as users during continuous service. The purpose of the present research is to study the delamination of flexible solar cells using the principles of fracture mechanics (cohesive zone and J-integral) and peeling test protocols.

To characterize this delamination, cohesive zone modeling was implemented because it can predict delamination in complex structures and the implementation is easy in finite element methods [45]. Cohesive zone relates the cohesive traction and the relative displacement of the cohesive surfaces (upper and lower surfaces). This displacement leads to physical growth when it reaches a critical value (peak cohesive traction(σ)). Figure 2.10 shows the cohesive zone ahead of the physical crack tip (bonded surfaces) and the increment of separation (δ) between each cohesive surface when the crack is propagated after the σ is reached.

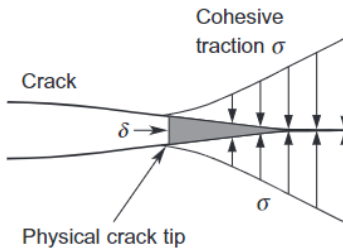


Figure 2.10. A cohesive zone ahead of a crack [46].

To measure the energy required to start the crack propagation, a peeling test was used to assess the failure of flexible laminates. It is extremely important to mention that peel test indirectly assess the toughness of the adhesive or interface because it measures the peel load per unit width. Indeed, this experimental method has the advantage of being very easy to perform and having a simple test setup. A large amount of analytical peeling model based on an energy balance was developed by different author [45] where they determine the fracture energy (G_a) using energy balance which will be used to validate the experimental measured peel force. In addition, J-integral approach proposed by Rice is covered here, so a two-dimensional crack propagation is compared with the cohesive zone model. J-integral represents the energy release rate at the crack tip that is path independent for a contour surrounding the crack tip (see Figure 2.11).

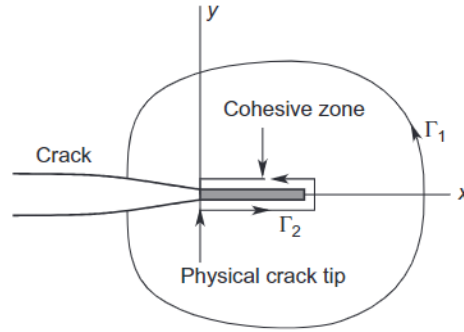


Figure 2.11. J-integral applied in two different paths [46].

2.6 Objectives

The main objective of the present work is to investigate and predict the delamination of interfacial layers of flexible solar cells through principles of fracture mechanics such as cohesive zone and J-integral both analytically and experimentally. Fracture mechanics principles will be applied to the peeling test and the main fracture energy parameter will be obtained using this process.

3. EXPERIMENTAL PROCEDURE

3.1 Overview

The solar panel used in this project is the portable Hanergy SP-08 flexible CIGS (see Figure 3.1a). This solar panel can provide a maximum power of 8W and an output voltage of 5V. It is made out of five different layers, with an efficiency of 17.3% [47]. This is due to its primary active layer (CIGS) and substrate. Improving the efficiency of this solar panel requires an understanding of how cracks are generated in its interface. The analysis is focused on the interface between two specific layers which were selected after an inspection in the solar panel. For the inspection, it is required to prepare rectangle samples using constant dimensions of 20 x 100 mm (see Figure 3.1b). Generally, CIGS solar cells use different techniques (co-evaporation or deposition), so each layer is added to the CIGS structure making a five-layer composition. This process creates several bonded layers without using an adhesive layer between them. In this project, it is required to create an initial crack between the layers of the solar cell. Different manufacturing processes make it difficult to separate the layers from each other. However, this specific panel has a front cover protection, which makes it easy to separate the protection layer from the rest of the layers. After the layer separation, two separated layers are created which needs to be analyzed. A scanning electron microscope was used to identify each layer composition. A uniaxial tensile test was ran at a constant speed of 10 mm/min to find the young's modulus and yield strength for each layer. It also was required that the test was analyzed both with and without an extensometer, so the results can be compared. A peeling test using different angles is implemented to obtain the force required to initiate the delamination between layers. All these processes were fundamental in order to obtain the energy required to start the delamination propagation at the interface of these two layers. A more detailed description for each process is included in the following section. The data is then collected very thoroughly, as detailed in section 3.4, so the results can be implemented in the numerical analysis using a commercial finite element analysis (FEA) software.

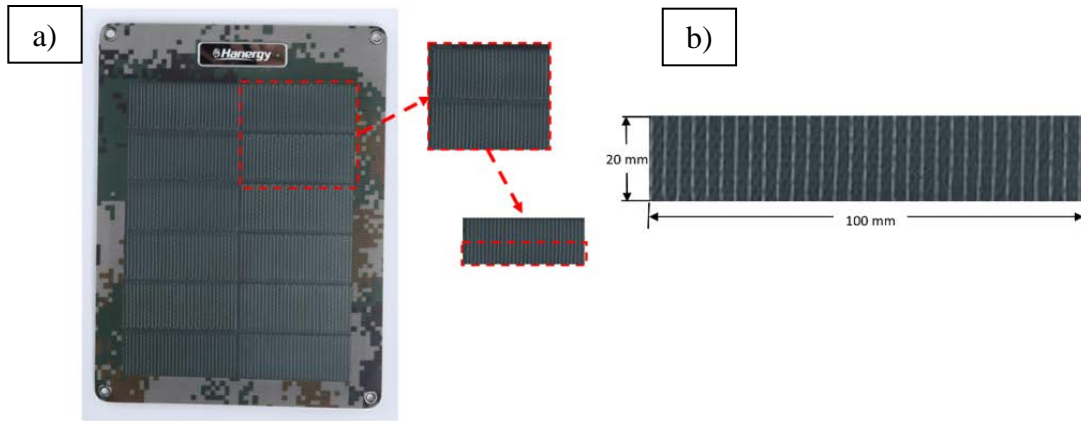


Figure 3.1. Flexible solar cell. (a) Hanergy SP-08 flexible CIGS. (b) Sample test for all experiments.

3.2 Orientation angle for the experiment

As stated previously, Hanergy SP-08 flexible CIGS solar panel were used for all experiments. This solar panel had twelve individual rectangular cells, which were divided in test samples of 100 mm length by 20 mm width (see Figure 3.1b). It was suggested by Moore and Williams [35] that angles between 45 and 135 degrees are necessary to calculate the fracture toughness in the peeling tests. They also mentioned that the 90-degree peeling test should always be one of the settings. In this experiment, 45, 60, and 90 degree angles were selected as the baselines in the MTS fundamental 90-degree peel fixture machine (see Figure 3.2). Five test samples were created for each angle orientations. The MTS machine measures the force required to peel any specimen. However, the factory default settings only allows the user to define one type of degree configuration, which was the 90-degree orientation. This mechanism employs precision bearings between the upper plate and lower plate of the grip, which creates a horizontal motion with minimal friction due to the precision bearings. The orientation cannot be changed, so it was necessary to design different 3D printed custom plates. The custom plates can change the orientation of the peeling test and can be easily incorporated in the MTS machine. The custom plates were created in Solidworks® and 3-D printed using Polylactic Acid (PLA) in a Maker Bot® printer (see Figure 3.3). Once these custom plates were designed and printed, it was possible to measure the force required for the peeling test at different angles.

The testing was maintained at a constant temperature of 24 °C to ensure consistency in the results. The test specimens were glued to the custom plates to avoid any increase in the measurements of the peeling force. After each test, the surface of each custom plate was completely cleaned to minimize any error caused by incomplete contact between the custom plate and the test sample.



Figure 3.2. MTS Fundamental 90-degrees peel fixture machine.



Figure 3.3. Custom plates for 45, 60, and 90-degrees.

3.3 Sample material

CIGS solar cells are generally made out of five different layers, which each have a thickness equating to microns [48]. The analysis can be made for the different layers, but the accessibility to them and its layer compositions are difficult to obtain. This is caused due to different techniques being used to manufacture the solar panel and the lack of a detailed layer composition by the manufactory company. Information was provided about the primary active layer (CIGS) of the structure, and the SS layer was seen acting as a back layer in the structure. The small thickness size of each layer, due to different co-evaporation or deposition techniques, causes difficulty in differentiating each layer. This problem was overcome by using a scanning electron microscope (SEM). The specimen (see Figure 3.1b) was analyzed in the SEM to obtain information about its composition. The SEM image in Figure 3.4 shows the cross-section of the CIGS solar cell. From this figure, it can be confirmed that there was no debonding at the multilayer film. After this confirmation, Figure 3.5 illustrated the solar cell composition, showing elements such as molybdenum (Mo), iron (Fe), chromium (Cr) and aluminum (Al). It is important to mention that the information about aluminum (Al) displayed in the SEM image was due to the sample holder used in the Phenom SEM. This material will not be considered within the analysis. Using this information, different layers, for instance, zinc oxide (ZnO), cadmium sulfide (CdS), the primary active layer (CIGS), and molybdenum (Mo) were labeled as the Mo layer.

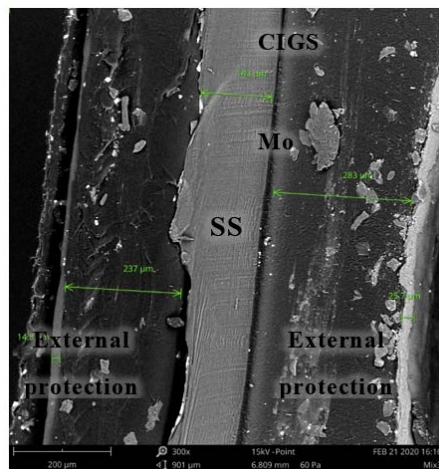


Figure 3.4 Scanning electron microscope (SEM) images of CIGS solar cells showing the cross-sections of the multilayer film.

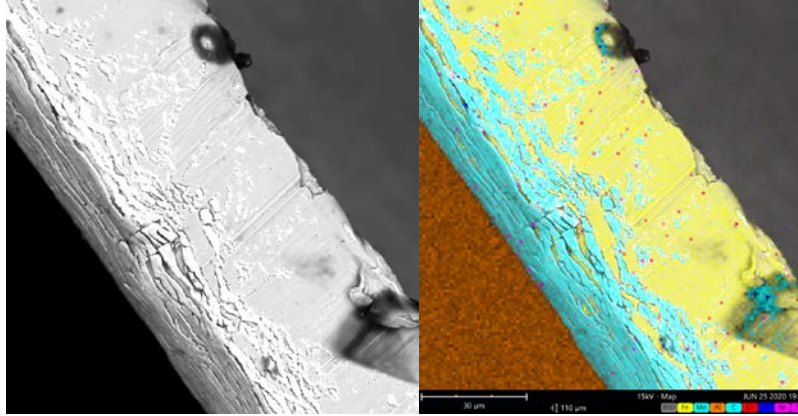


Figure 3.5. High resolution scanning electron microscope image (SEM) of a CIGS solar cell showing Mo/SS interface.

The reason for defining multiples layers as the Mo layer is due to the small thickness of each layer, as well as the typical layer composition of a CIGS solar cell (see Figure 3.6). Beneath the Mo layer in Figure 3.6 is the stainless steel (SS) substrate. Due to two important factors, the interface between the Mo and SS layer was the focus of attention in this study. The first factor was the easy separation between layers. The specimen gets delaminated without using an excessive force. The separation did not require any thermal stress or loading types in order to separate these two layers. In this case, delamination occurred in two different interfaces when a force was applied at the peel arm and the SS layer was fixed: 1) Delamination between Mo and SS. 2) Delamination between flexible solar protection and ZnO. In section 3.6, there is a more detailed description for the analysis of the interface between the Mo and SS layers. However, the second interface between flexible solar protection and ZnO is not covered in this project, because the interface related to Mo is much more critical than the interface between flexible solar protection and ZnO in terms of performance and durability.

This leads to the second factor, which is related to the solar cell composition. The CIGS solar cell has multiple layers of different materials. Mo back contact is one of these layers and it is used quite frequently in CIGS-based solar cells [49]. The selenization of Mo layers at different temperatures and for different durations can develop high-efficiency CIGS solar cells on a variety of back contact materials [50]. The MoSe₂ layer at the CIGS/Mo interface, for instance, contributes to the improvement of adhesion at the CIGS/Mo and it facilitates a quasi-ohmic electrical contact (low resistance) across the CIGS/Mo interface. Different techniques use Na-doped Mo layer to

create a diffusion barrier against impurity ions originated from the substrate (SS). This barrier increases the efficiency of CIGS solar cells fabricated on SS substrates, which is low compared to the efficiency in conventional CIGS solar cells on a soda-lime glass (SLG) [51]. Another way to improve the performance in Mo layer is to use a bilayer structure. Mo bilayer, for example, is implemented in CIGS solar cell structure to improve the adhesion and reduce its ohmic resistivity [52] [53]. Misra et al. [54] also demonstrated the improvement of adhesion and mechanical stability by exploring a dip coated SiO_2 in the interface layer between Mo back contact and substrate (SS).

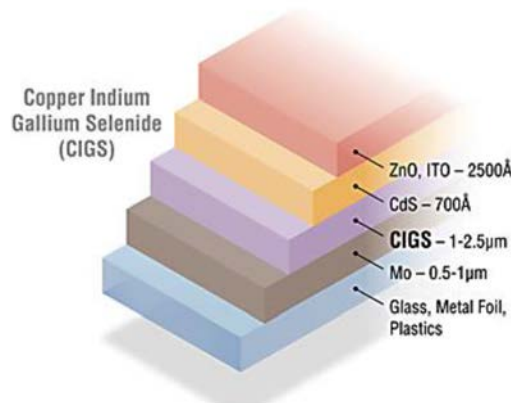


Figure 3.6. Layer composition of a CIGS solar cell [55].

Stainless steel (SS) is the second layer of interest in this project due its low cost, and excellent thermal and chemical stability [48]. Indeed, metal foil substrates usually are implemented instead of soda-lime glass or plastic for CIGS flexible solar cells [7] due to several advantages. Morán et al. mentions some advantages when SS is used as a flexible substrate related to durability, greater process temperature capability, dimensional stability, and superior barrier oxygen and water barrier characteristics [56]. It also reduces the solar cell weight and fabrication cost by roll-to-roll mass production [57]. Despite the advantages of SS in flexible solar cells, there is impurity between the substrate (SS) and the absorber (CIGS layer) which significantly reduces the conversion efficiency [58]. The solution for this issue is the development of barrier layers in order to increase thin-film adhesion and protect the device from the diffusion of moisture and impurities [51] [58] [59] [60]. The study of the interface between these two layers can contribute with the

solar cell industry because one goal of this research is to find the delamination energy (energy release rate) between Mo and SS through peeling experiments. This can be used as reference for possible improvements or to create specification which can avoid this delamination.

Before the material properties for the sample were obtained, it was important to confirm whether the interfaces were Mo and SS because the assumptions were based on a typical solar cell composition (see Figure 3.6). There are five layers in the solar structure. When the SS layer is peeled away from the other layers, the following layer in the five layers composition is Mo. Figure 3.4 and Figure 3.5 have shown that the layer after the SS layer is the Mo layer. However, it was necessary to analyze if there was material remaining from the other layers after the peeling process. Figure 3.7a shows that after a peeling test was completed, there was material attached in the peeling arm. This material was analyzed, and it was confirmed that the material remaining in the peel arm was Mo. Figure 3.7b also shows that the material remaining in the SS surface contains remnants of different materials, which represent the stainless steel chemical composition. There was not presence of materials from other layer compositions such as zinc (Zn) from the ZnO, or cadmium (Cd) and sulphur(S) from the CdS layer. There is not cadmium (Cd), copper (Cu), indium (In) and gallium (Ga), but there is a minimal presence of selenide (Se) from the CIGS layer on the SS surface. The SEM analysis confirms again that the interface for this study is the fused area of the Mo and SS layer. All settings (45, 60, and 90 degrees) show similar conditions displayed in Figure 3.7a and Figure 3.7b. Appendix A shows a more detailed composition for this interface.

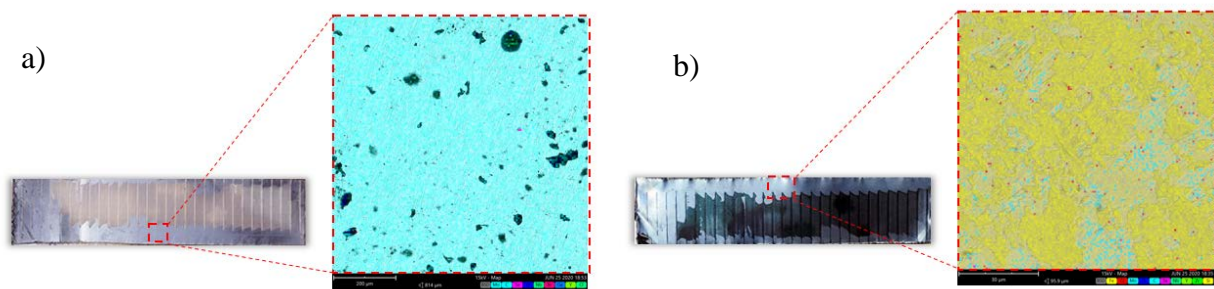


Figure 3.7. Specimen after peeling test. (a) Peel arm(presence of Mo), (b) bottom layer(presence of Mo and other materials in the film).

3.4 Procedure for measuring the mechanical properties of the peel arm

Rectangular samples of 100 mm length by 20 mm width were used in this part of the experiment. The Mo layer of the specimen was manually separated from the SS layer. The separation was made by hand, so any external stress generation is avoided as much as possible. After the separation of the Mo layer, it was confirmed that this layer contained presence of molybdenum (Mo) material on its surface. It was required to find some additional material properties such as young's modulus and yield strength. Following the examination, the uniaxial tensile test was carried out five times at 10 mm/min with a constant temperature of 24 °C, so these additional properties can be experimentally determined. It also was required to include an extensometer in this tensile test, so results with or without the extensometer will be commented. Figure 3.8 shows the failure in the peel arm a under uniaxial tensile test. An extensometer was used to measure the strain deformations necessary to define the elastic deformations. A non-contacting type was suggested to enable a clear definition of the plastic region of the deformations [35]. A contact extensometer was available in the lab, so it was implemented in each test instead of using a non-contact type. The localization of the plastic region was defined within the working range of the contact extensometer (25.4 mm). A different test was also carried out using a simple setting in the MTS software without the extensometer, which requires some specimen information such as width, thickness, test rate, and grip separation (see Figure 3.9). Both sets of collected data are discussed in the following chapters, and one of these collected data will be used as reference for the simulation part of this project.

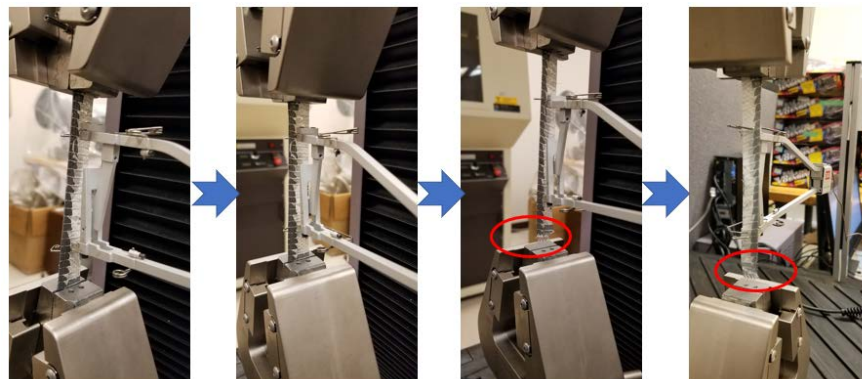


Figure 3.8. Uniaxial tensile test using a contact extensometer.

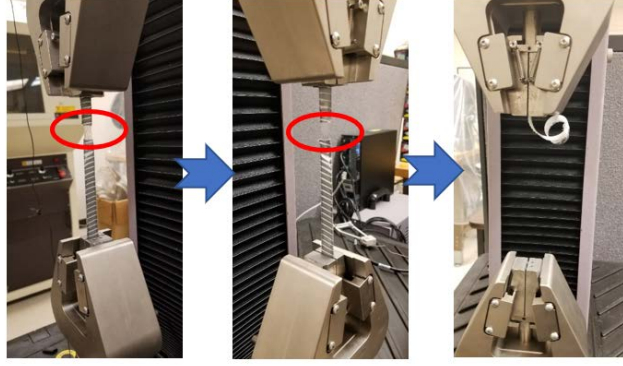


Figure 3.9. Uniaxial tensile test without contact extensometer.

The data collected in the uniaxial tensile test was plotted as a stress-strain curve, so the young's modulus(E) and yield coordinates (ϵ_y, σ_y) were found. The yield strength was obtained by fitting a bilinear elastic-plastic curve for the stress-strain plot (see Figure 3.10). These parameters provide the required information in order to calculate the energy release rate, so the following instructions were followed once the data was collected and plotted:

1. Create a line that passes through the linear elastic region of the stress-strain curve.
2. Create a line starting from an estimated yield point that ends at approximately 10 times the yield strain (This line represents the initial plastic region of the curve).
3. The interception of these two lines defines the yield coordinates (ϵ_y, σ_y).

These instructions reduce the complexity of finding the yield coordinates due to the sample being part of a flexible solar panel. The solar cell layers obtained from the solar panel had a protection cover made of flexible plastic. The deformation in the tensile test is linearly elastic initially, but the maximum strength is not visible in the stress-strain curve. The sample does not fracture completely, it does not resist the deformation like metals, and it tends not to break immediately. In this case, the yield coordinates can be a challenging process, which can produce a discrepancy in energy calculations. This is the main reason why we use the previous instructions and the following equation. This equation is a correction for the plastic deformation used in the protocols presented by Moore and Williams [35], which is used to verify the data accuracy.

$$CFPD = \left(\frac{G_{db}}{G} \right) \times 100 \quad (20)$$

The correction factor for the plastic deformation (CFPD) relates the plastic work done in the bending of the peel arm (G_{db}) and the total input energy (G). This ratio should be as small as possible, so the error in the energy release is insignificant.

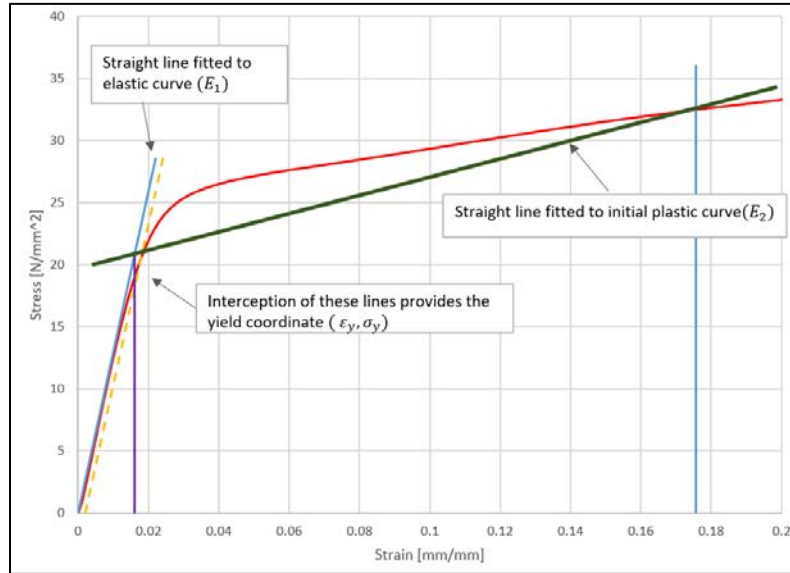


Figure 3.10. Tensile test for the peeling arm.

3.5 Procedure for measuring the properties of the bottom layer

The bottom layer had a protection layer, which was carefully separated from the stainless steel layer (see Figure 3.11). The dimensions for the stainless steel were 20 mm width, 100 mm length and 0.05 mm thick. The uniaxial tensile test used in this procedure had the same condition as it was implemented in the peeling arm test with and without an extensometer (10 mm/min at 24 °C). Young's modulus for each test was recorded, so they can be used in each numerical analysis in order to simulate a real condition in the experiment.

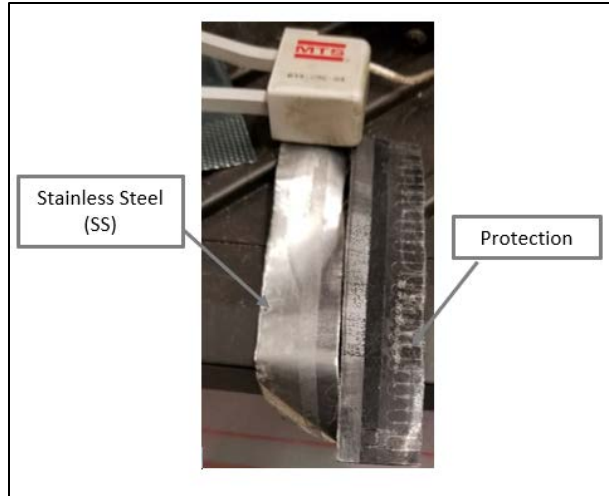


Figure 3.11. Bottom layer with protection.

3.6 Procedure for the peeling test

Figure 3.12 shows the specimen configuration during a 90-degree peeling test in an MTS machine. The test is used to obtain the force required to delaminate the specimen selected. The specimen dimensions were kept the same as they were used in the tensile test of the peel arm and bottom layer. A region of unadhered material between the Mo and SS layer interface was created, and this region was known as initial crack (30 mm). Five specimens were tested for each set of conditions (45, 60, and 90 degrees), and the force –displacement curve was recorded during the initiation and propagation of the delamination. Initial results show that there are two situations in the collected data, which could not be controlled during the experiment.

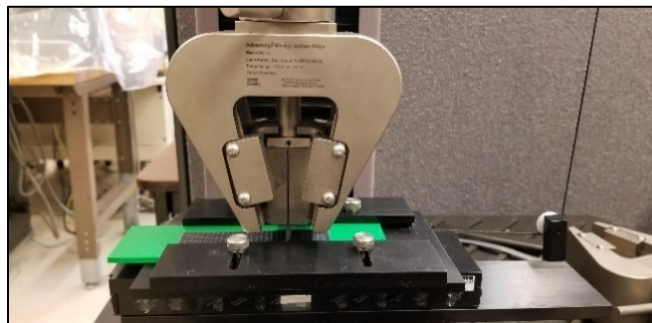


Figure 3.12. Fixed arm peel fixture with linear bearing system showing a 90-degree peel angle.

The first situation generates a plot with two different types of peel traces (see Figure 3.13). The plot indicates that these traces depend on the material remaining in one of the surfaces from either the peel arm or SS layer after the delamination. The plot also depends on how the material is distributed. When the peel arm keeps a small amount of material on its surface after the test, the amplitude increases during the delamination process. At approximately 26.75 mm of delamination in Figure 3.13, the amplitude is reduced drastically due to the increment of material remaining in the peel arm. The peeling force in each experiment, which produce an interfacial delamination, depends on the amount of material (ZnO, CdS, CIGS (primary active layer), and Mo) remaining in the peel arm. In Figure 3.13, the remarkable difference between amplitudes can be seen at approximately 26.75 mm, but this displacement is different in each test. The locations of the remaining material also plays an important factor in the amplitude change. The peel arm in Figure 3.13 has material remaining in the middle of its surface, which coincides with the decrease in peel force. This abrupt decrement and increment in amplitude is due to the localization of the remaining material which could not be controlled during the experiment.

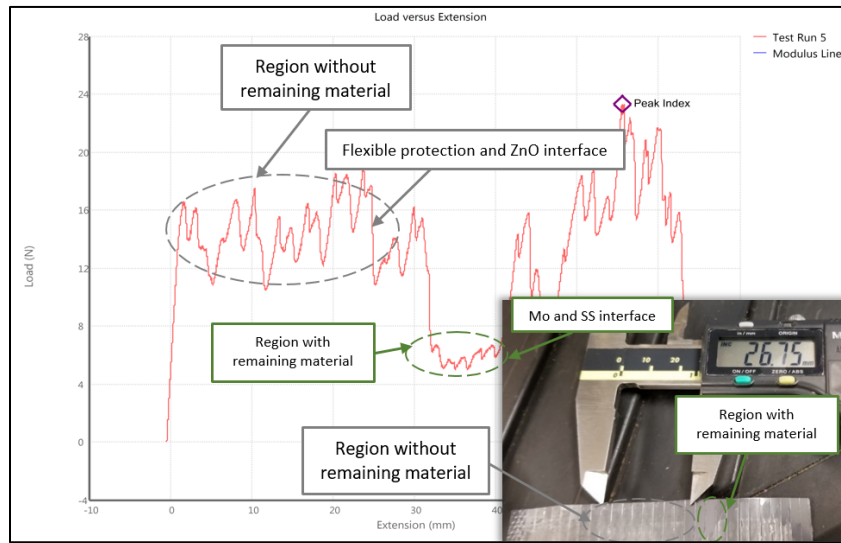


Figure 3.13. Force vs displacement for 90-degree peeling test.

The second situation can be easily distinguished due to the small variation of amplitude during the complete deboning process. In Figure 3.14, the amplitude variation is small compared with Figure 3.13. Visually, the amplitude variation can also be distinguished due to the remaining

material in the peel arm and SS surface. In this case, most of the material (ZnO, CdS, CIGS and Mo layers) were remaining on the SS surface, and the material was located at both sides of the peel arm. About 80 percent of the material was visualized on the surface of the SS layer (see Figure 3.14). This peculiarity in the experiment creates a plot force-displacement, which represents the force required to start the delamination process between the flexible protection and the ZnO layer. In the case that the curve has a remarkable increase or decrease in amplitude, the experiment was repeated until the change in amplitude could be avoided.

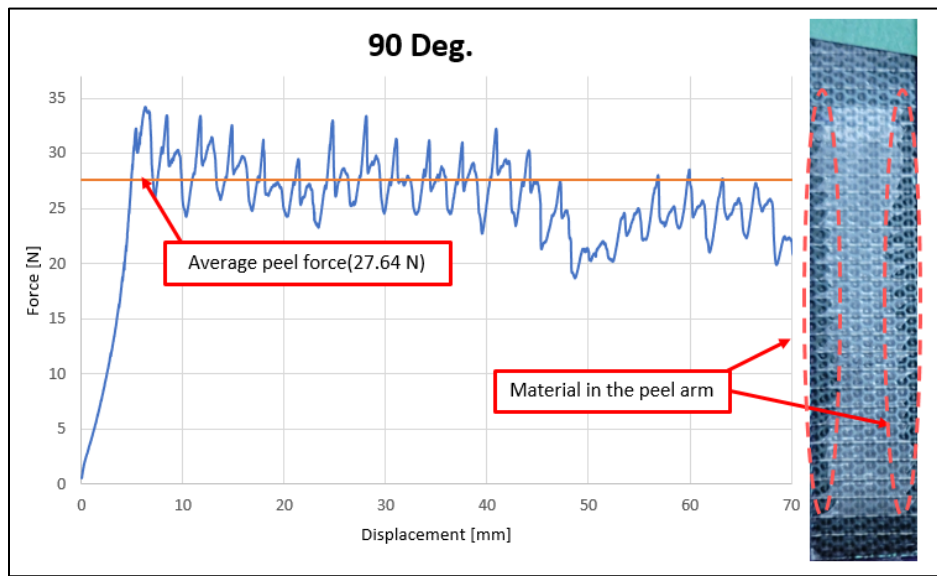


Figure 3.14. Average peel force vs displacement in 90-degree peeling test.

The goal of the project is to analyze the interface between the Mo and SS layer, but these two situations in the experiment could not be controlled. In order to achieve consistency for the results, all the data was obtained from the specimens which behave according to the second situation. This situation was more present in the experiment than the first situation, with a massive increase or decrease in amplitude. These collected data were later analyzed and related to the goal of the project. It was required to make an estimation, so that the peeling force for the interracial delamination between Mo and SS could be obtained. In the second situation presented in the test, the majority of delamination (~80%) occurs in the interface between flexible protection and the ZnO layer. A preliminary result showed that the force in this interface was two times greater than the Mo and SS interface as shown in Figure 3.13. Due to the unexpected change in interface during

the experiment, the delamination force in the Mo/SS interface (F_R) would be obtained by using the following formula:

$$F_{avg} = \frac{Interface1}{100} (2F_R) + \frac{Interface2}{100} (F_R) \quad (21)$$

F_{avg} is the average delamination force measured in the peeling experiment for each orientation angle. It represents the measured delamination force between flexible protection and ZnO layer during the peeling experiment. Interface 1 and Interface 2 represent the percentage of material related to each interface after the delamination process. F_R represents the desired delamination force between the Mo and SS layer, which was experimentally found to be half as the delamination force between flexible protection and ZnO (Figure 3.13) Interface 1 corresponds to the flexible protection and ZnO interface, and Interface 2 corresponds to the Mo and SS interface. The first term of the equation represents the flexible protection and ZnO interface. The second term represents the Mo and SS interface. This second term is half the value of the first term in the equation. After several tests, percentages of Interface 1 and Interface 2 were found to be 80% and 20% respectively from the experiment as shown in Figure 3.13. This procedure was required in the analysis and it was successfully implemented in order to get the energy release rate of the Mo/SS interface in chapter 5.

4. SIMULATION PROCEDURE

4.1 Finite element simulations

To evaluate the delamination force of the interface between Mo and SS layers sample under peeling test, finite element (FE) simulations were performed using COMSOL Multiphysics. The thickness for the defined Mo and SS layer were 0.84 mm and 0.05 mm respectively, with a width of 20 mm for both Mo and SS layers. The length of the specimen was set to 100 mm. The material properties for the simulation were obtained from published journals and experimentation, which are all listed in Table 2. The FE-model for a 90-degree configuration was compared with the experimental data. Since all parameters of the FEM simulations could not be obtained from the experiments, some were estimated. The material parameters required for analysis were difficult to obtain. The yield coordinates obtained from the experimental stress-strain curve (see Figure 3.10) could vary. It was difficult to differentiate the elastic-plastic region in the curve. If there is a remarkable discrepancy in the results, the material parameters could be adjusted to better fit the experimental data.

Table 2. Mechanical and physical properties of materials used in this study.

	Mo	SS
Young's modulus (MPa)	1295[experimental]	90529.88 [experimental]
Density (g/cm ³)	10.2 [61]	7.8 [61]
Poisson's ratio	0.25 [61]	0.32 [62]
Coefficient of thermal expansion ($10^{-6}K^{-1}$)	4.8-5.9 [63]	10-15 [61]

4.2 Peeling simulation using COMSOL software

The geometry of the solar cell specimen makes it very suitable for modelling using a simple CAD software, because the specimen geometry consists of two layers sharing the same interface. Dimensions are described in the previous section, with more detailed descriptions in chapter 3.1

(see Figure 3.1b). This geometry is implemented in two types of simulations using COMSOL, so the delamination can be predicted. The first type of simulation used the J-integral in a two-dimensional (2-D) geometry, which can calculate the energy release rate and the separation displacement required to start the delamination process. The second type of simulation used the cohesive model in COMSOL, which runs the virtual peeling test using parameters such as: tensile and shear strength, penalty stiffness, mode I and II critical energy release, and exponent of Benzeggagh and Kenane(B-K) criterion. These simulations are explained more in detail in the following sections, and the results using 90-degree configuration are shown in chapter 5.

4.2.1 J-integral using the COMSOL software

A two-dimensional geometry and contours around the crack were created in order to compute the J-integral. The evaluation of the J-integral for four contours is shown in the Figure 4.1, which enclose the top and bottom layers. The integral is evaluated for the four contours. This procedure can be implemented in different sets of conditions (45 deg., 60 deg., 90 deg. and so on) if the user requires. The simulations had two boundary conditions. First, a fixed boundary condition was applied to the bottom layer (SS). Secondly, an incremental displacement was applied to the edge of the top layer (Mo layer) ranging from 0 to 20.6 mm with an increment of 0.1 mm. After applying the boundary conditions to the 2-D geometry, COMSOL calculates the energy release rate as a function of the separation displacement. These results are used to estimate the critical separation value (δ_m) (see Figure 2.2, chapter 2.2) between surfaces where the cohesive traction is zero. The crack is initiated at this critical value, before the material begins a process of irreversible delamination.

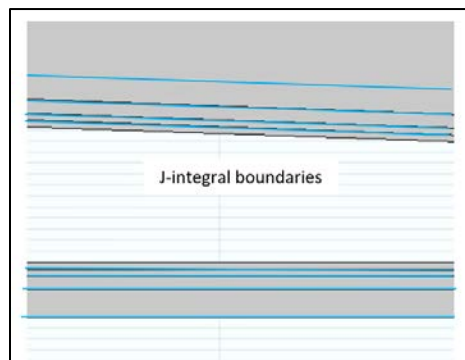


Figure 4.1. Contour around the crack tip used in the definition of J-integral.

4.2.2 Three-dimensional (3-D) model of the sample test

To simulate the delamination of the interface between Mo and SS layers of the solar cell, a three-dimensional geometry was carefully modeled, following the specification described in section 4.1. The geometry consists of one horizontal layer with 100 mm in length sharing an interface with a second layer. The design of the second layer includes a 90-degree bent section and a horizontal section, which simulate a more realistic specimen configuration of the peeling test (see Figure 4.2). A special focus on the mesh generation was considered between the sections where the layers are bonded because these layers will be separated after applying certain conditions. Two approaches were initially considered for the delamination simulation. The first approach uses a load-control method in which a force was applied to one face of the upper layer of the peel arm in the z- direction. This force constantly increases until the delamination is started.

The second approach uses a displacement-control method. The displacement was applied at the same place and direction from the previous approach, which was increased progressively until the delamination was started. Ideally, the peeling force (a force required to generate a delamination) should be obtained using both methods from the reaction forces tool in COMSOL. However, the first approach was discarded due to possible convergence issues. Once the peak force is reached, there is no possibility to continue the analysis [64]. The final conditions in COMSOL used a prescribed displacement, which was gradually increased using the auxiliary sweep tool of the COMSOL stationary solver. A fixed support is then applied in the bottom layer, so the reaction force can be measured.

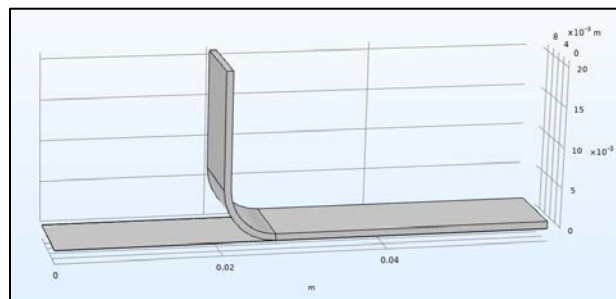


Figure 4.2. Configuration for 90-degree peeling test.

4.2.3 The cohesive zone model simulation in the COMSOL software

The model uses a cohesive zone model, which implements a bilinear traction-separation law. In the COMSOL software, the traction has a constant and linear increment with a penalty stiffness K . This increment stops when the failure initiation displacement is reached. After this point, the crack is initiated and the material starts a process of irreversible damage where the cohesive traction is zero [65]. The penalty method was selected over the augmented Lagrangian method to solve contact problems due to the tradeoff between accuracy and stability. Finding the correct values for the penalty stiffness was a difficult procedure due to the convergence problems in the Newton iteration. Song et al., mentions the importance of selecting the correct value for the penalty stiffness, because this factor can prevent numerical problems in traction –separation response [66]. High values of the penalty factor can lead to convergence problems. This is due to the fact that it was not required to adjust the penalty factor as the solution progresses in the simulation because initial results did not have convergence issue.

Figure 4.3 represents the bilinear traction-separation law used in COMSOL. The penalty stiffness has a linear increment until it reaches its maximum value corresponding to δ_c . This maximum value represents the normal strength required to simulate the peeling test. In order to obtain this value, some estimations were required based on experimental results and COMSOL observations for the 90-degree peeling test. The experimental results showed that the delamination occurs around 1mm and the crack tip displacement (in COMSOL observations) was half of the displacement measured at the tip of peeling arm. Taking into account these considerations, the critical separation (δ_m) is assumed to be 0.5 mm and the initial separation is assumed to occurs at $\delta_m/2$. The area of the triangle created between the critical separation and the normal strength represents the energy release rate (218.43 J/m²). This information was used to calculate the normal strength (8.74×10^5 N/m²), and the penalty stiffness could be estimated. The shear strength also was estimated by assuming that the tensile yield strength was between 60 and 90 percent of the tensile strength [67]. The shear strength was 67 percent of the normal strength. This principle was used once more for mode II critical energy release (G_{II}), which uses 67 percent of mode I critical energy release (G_I). The Exponent of Benzeggagh and Kenane (B-K) criterion of 2.284 was taken as reference from the cohesive model found in the COMSOL's application libraries. These parameters were used for the traction-separation law available in the COMSOL software, so the experiment could be recreated.

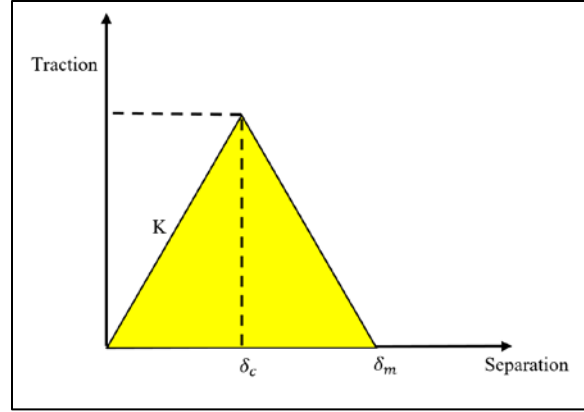


Figure 4.3. Traction-separation law used for the estimation both normal strength and penalty stiffness.

A contact pair node available in COMSOL was implemented to specify two boundaries that cannot penetrate each other under deformation. The selection of source and destination in a contact pair in COMSOL was based on the fact that the source must be the stiffer layer and the layer which is constrained by a fixed constraint. Due to these two conditions, the upper surface from the SS layer was selected as the source boundary and the lower surface from the Mo layer was selected as the destination boundaries (see Figure 4.4).

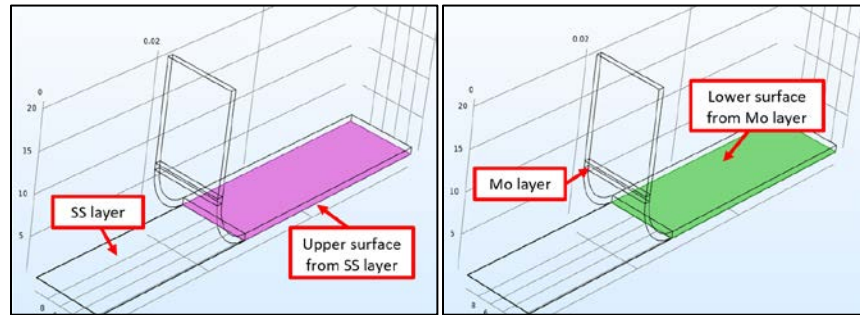


Figure 4.4. Contact pair: a) Source boundaries. b) Destination boundaries.

4.2.4 Mesh generation

A mesh refinement was considered in the simulation. A smaller mesh size was generated ahead of the crack tip (0.51 mm), and the rest of the peel arm had a different mesh size 1.02 mm (see Figure 4.5). These values were selected after conducting a mesh sensitivity study which

demonstrated that changing the mesh size does not affect the result. Special care was taken in the circular region of this model. Multiple faces were used for creating the mesh in the peel arm, so there are not discontinuities in the mesh which can lead to a numerical issue during the simulation. The generated mesh has a 3640 number of elements, and takes around five hours to complete due to the small element size. The element size could not be increased because the bottom layer had thickness of 0.05 mm, but the mesh size was selected after conducting a mesh sensitivity study.

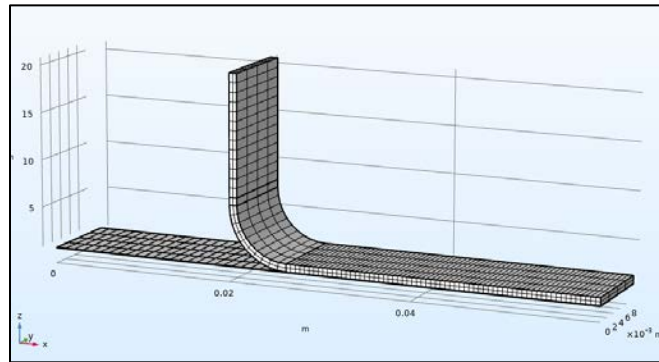


Figure 4.5. Mesh generation for a realistic peel test in 90-degree.

5. RESULTS AND DISCUSSION

5.1 Peeling arm data

The specimens were prepared according to the specifications described in chapter 3. The uniaxial tensile test was carried out at 10 mm/min with and without a contact extensometer. Figure 5.1a shows the collecting data and its failure for a simple tensile test without using an extensometer. It shows some important parameters needed for the analysis. Even though all protocols in chapter 3.2 were followed, it was difficult to differentiate the yield strength due to the material composition. The exact point where a line stress-strain stops being linear is not so visible in each collected data, so it was required to make an estimation.

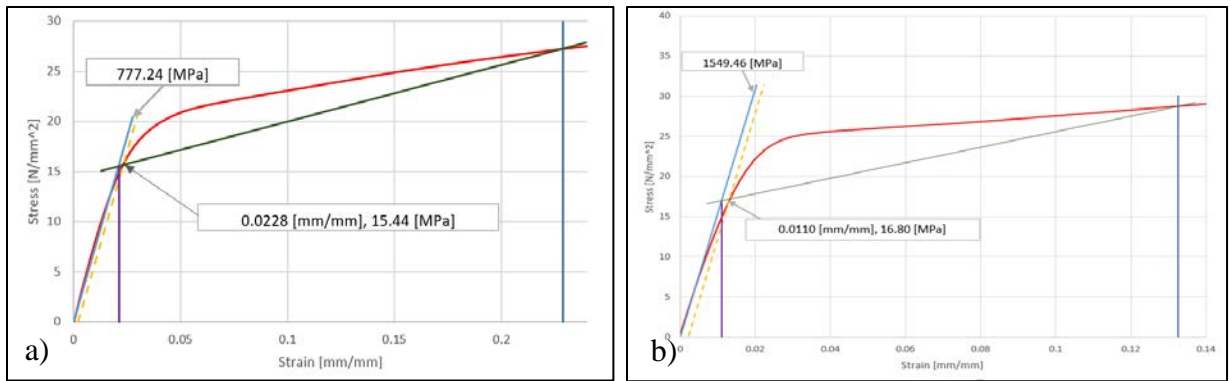


Figure 5.1. Important Parameters in the Peel Arm. (a) Without extensometer, (b) Using a contact extensometer.

The clip-on extensometer, which has a maximum displacement of 25.4 mm, was used for high precision strain measurements. The result for the first experiment using this contact extensometer can be seen in Figure 5.1b. Important parameters are shown in appendix B, where it can be seen some marked differences between the experiments with and without a contact extensometer in terms of magnitude. A compilation of the mechanical properties for each testing is presented in Table 3. Mechanical properties for the peeling arm., which shows a large degree of scatter on the measured young's modulus. Results without an extensometer have a range of values between 700 and 1000 MPa. On the other hand, data obtained with the extensometer displays a significant increase in the young's modulus, with a range between 900 and 1600 MPa. All initial

settings, such as initial speed, dimensions for the specimen and extensometer gage length (for contact extensometer) were the same for both types of testing, but differences in the results could not be avoided.

Table 3. Mechanical properties for the peeling arm.

Without Extensometer				With Extensometer		
Peel Arm	ϵ_y (mm/mm)	σ_y (MPa)	E (MPa)	ϵ_y (mm/mm)	σ_y (MPa)	E (MPa)
Test 1	0.0228	15.44	777.24	0.0110	16.80	1549.47
Test 2	0.0182	13.43	742.78	0.0161	20.86	1295.84
Test 3	0.0200	14.91	742.79	0.0141	18.63	1315.44
Test 4	0.0186	13.69	743.87	0.0183	20.41	1201.96
Test 5	0.0268	19.75	918.96	0.0130	13.34	996.76

Yield coordinates (σ_y and ϵ_y) do not differ by more than 29.30% for yield stress (σ_y). A 33.33% difference for yield strain (ϵ_y) was also determined. These percentages were taken from test 1 through test 5 with and without an extensometer. From all the available data, results using a contact extensometer were selected as reference material properties for the numerical solution. The reason of taking this collected data is due to the high precision strain measurements in the device. Data from test 2 (with extensometer) was used in each simulation as peel arm information. This decision was taken after the data in table 3 was analyzed. Two of the five tests had similar results in terms of yield strength and young's modulus. This was the reason why test 2 was selected as material properties in the analyses. The average values of all experiments could not be utilized because the energy release calculation takes into account all of the stress-strain curve. All properties from test 2 were chosen such as young's modulus of 1.295 GPa, yield strength of 20.86 MPa and the stress-strain data.

5.2 Obtaining parameters for the bottom layer

The uniaxial tensile test was used again in the analysis for the bottom layer. This test had the same conditions as it was used in the analysis for the peel arm, and Table 4 summarizes all experiments with and without an extensometer. Appendix C shows the information for all test. Even though the conditions and dimensions were the same between the uniaxial tensile test with

and without extensometer, Table 4 shows how they differ from each other. Values in the test without contact extensometer are not used in the analytical solution because there is more precision in the data collected when the test is using a contact extensometer. The results show that the material is too sensitive and any minimal variation in the initial conditions can have a huge effect in the collected data. The young's modulus of 90529.88 MPa was the average value taken from the test with an extensometer and a yield strength of 341.43 MPa. In this case, the average values could be taken from all experiments because it is only necessary to use these two values instead of using the stress-strain data from each experiment.

Table 4. Information for the Bottom Layer (SS)

	Without Extensometer		With Contact Extensometer	
Test	$E[MPa]$	$\sigma_y (MPa)$	$E[MPa]$	$\sigma_y (MPa)$
Test 1	34605.35	380.164	178839.2677	347.77
Test 2	45382.65	365.4901	92334.90476	333.1159
Test 3	59313.91	350.3062	55176.53994	343.861
Test 4	56151.94	301.5416	39543.05284	380.95
Test 5	84184.78	520.0578	86755.6701	301.467

5.3 Peeling test data

The force-displacement curves were obtained, and the critical separation values were recorded. The experiment was repeated several times, as it was explained in section 3.6. This was done so that abrupt increments in amplitude could be avoided. Figure 5.2 shows the result for a 90-degree peeling test, as well as the average force for the delamination process. Visual observations in the results indicated that the force increases in different locations, and the amplitude changes in some regions. Inspections made in the specimens after the peeling shows that the amplitude increases when there is a small amount of remaining material in the peel arm (see Figure 5.2). This visual inspection seems to explain the increment and decrement in amplitude depending on the material (ZnO, CdS, CIGS and Mo layers) remaining in the peel arm. The behaviors displayed in Figure 5.3a and Figure 5.3b also show the uncontrollable amplitude increment and decrement in 45 and 60 degrees orientations respectively. The material remaining

in figures 5.2 and 5.3 are located at both sides of the peeling arm. These characteristics were present in all specimens reported here, so the force average was obtained.

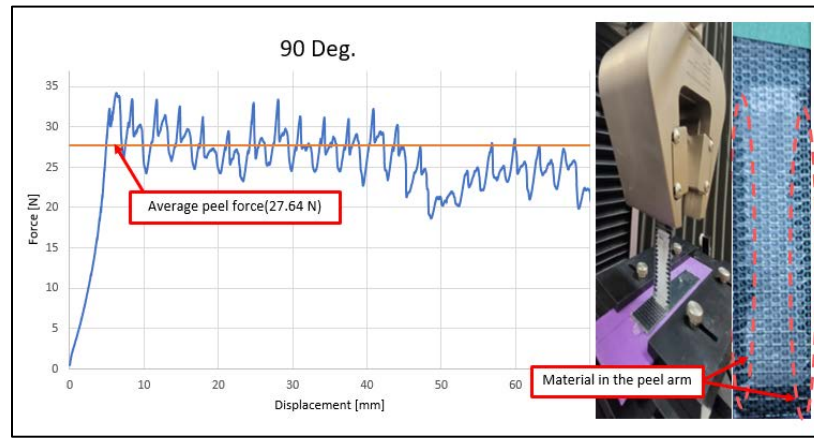


Figure 5.2. Force vs displacement for 90-degree peeling test.

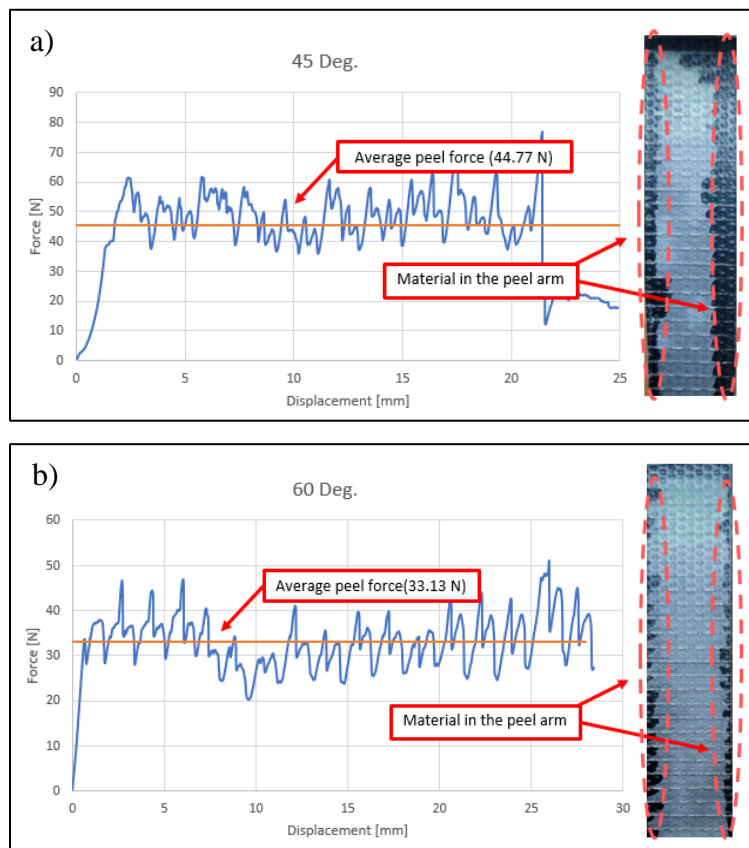


Figure 5.3. Force vs displacement. (a) 45-degree peeling test. (b) 60-degree peeling test.

Figure 5.4 shows all experimental settings for different peel angle configurations, and the initial crack manually generated. The initial crack has a length of 30 mm, and it was included in all tests. Table 5 summarizes the force required for starting the debonding process, and it reports some important differences between each test. It is essential to mention that the forces reported in Table 5 mostly correspond to the interface between the plastic flexible protection and ZnO.

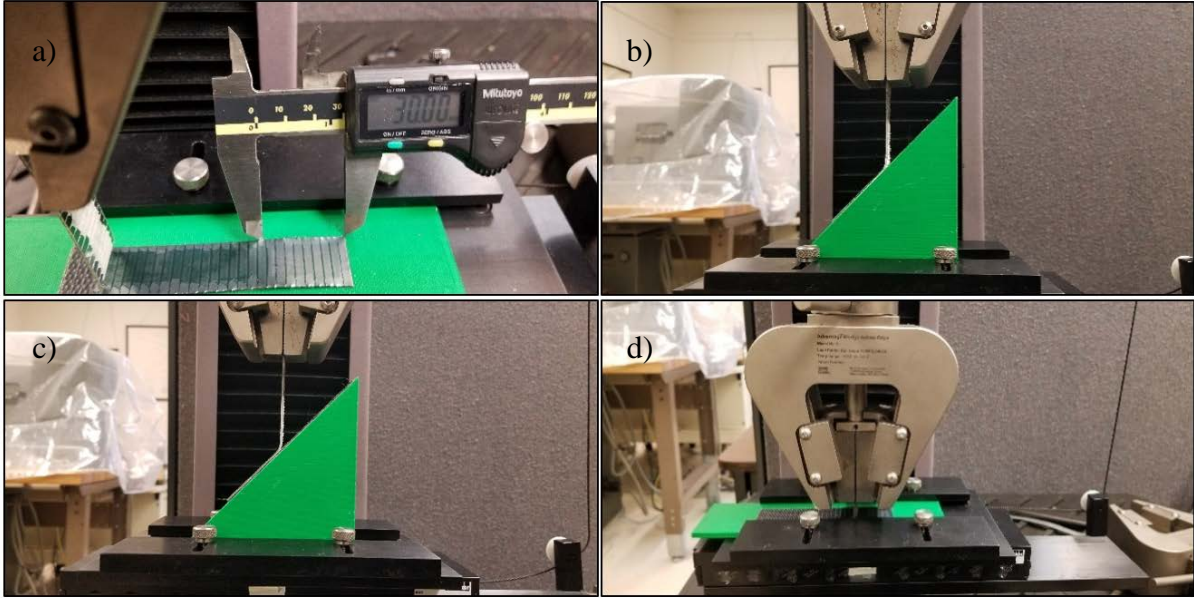


Figure 5.4. Peeling settings. (a) Initial crack, (b) 45-degree, (c) 60-degree, and (d) 90-degree.

Table 5. Peel Results for flexible protection and ZnO interface for multiple angle configurations

Peel Force (N)			
	45 Degrees	60 Degrees	90 Degrees
Test 1	44.77	35.59	27.65
Test 2	28.31	27.36	25.32
Test 3	58.40	37.62	27.64
Test 4	48.88	33.13	17.65
Test 5	48.84	37.03	13.94
Average Force	45.84	34.14	22.44

These collected data for different peel angles exhibit different types of peel force traces, which can be seen more in detail in appendix D for all configuration angles. An important trend

that should be noted is that the force required to start the delamination is reduced as the angle increases. The average peel force for all configuration angles, for instance, displays values in a descending order as it can be seen Figure 5.5. In this collected data, the 45-degree peeling test requires more force than the 90-degrees peeling test.

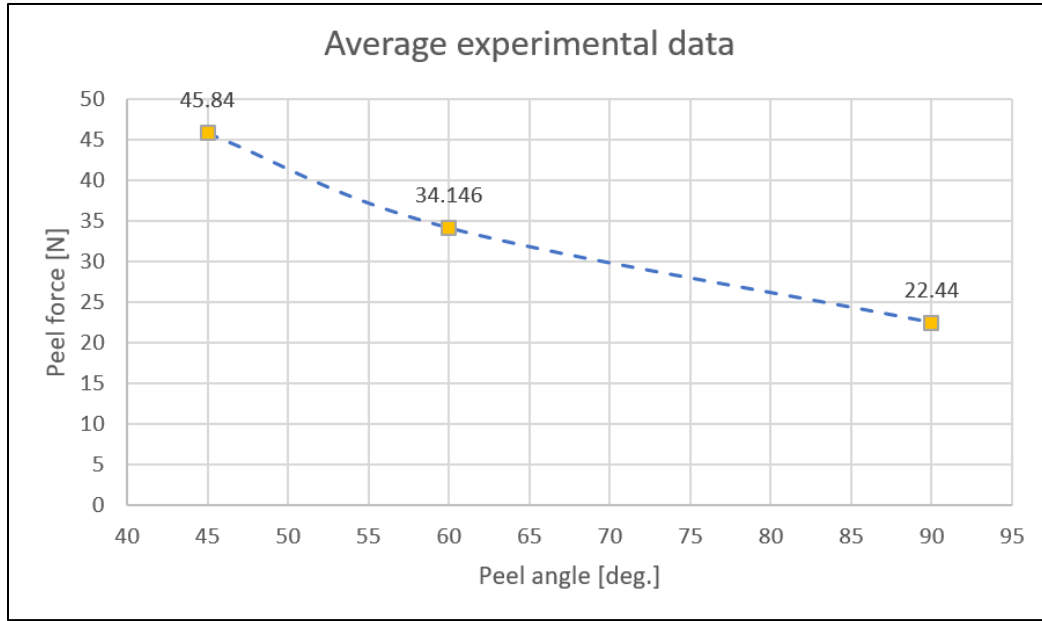


Figure 5.5. Average peeling force vs peel angle.

The average forces taken from Table 5 and equation 21 explained in section 3.6 were used to estimate the peeling force in the interface Mo/SS . Table 6 summarizes the estimated values, which will be used in the energy release rate calculations. The following equation used the information for the 90-degree peeling test. The same procedure was used for 45 and 60 degrees.

$$22.44 \text{ N} = \frac{80}{100} (2F_R) + \frac{20}{100} (F_R) \quad (21)$$

$$(F_R) = 12.46 \text{ N}$$

Table 6. Peel Results for Mo and SS interface for multiple angle configurations

Peel Force between Mo and SS interface (N)		
45-degree	60-degree	90-degree
25.46	18.96	12.46

5.4 Energy release rate

The energy release rate was calculated using the equations in section 2.4, which were incorporated in the program created by the Imperial College of London called ICPeel. This program uses properties of the peel arm and several highly non-linear equations to obtain the total input energy (G), energy dissipated during bending of the peel arm (G_{db}), and the fracture energy (G_a). Stress-strain data from test 2, using a contact extensometer, was used as the material properties for the peel arm. The average peeling forces in Table 6 were also included in the calculations for the analysis between the Mo and SS interface. Values used as inputs are summarized in Table 7. The results show that the total energy is directly proportional to the peel angle orientation. It also shows that the loading and unloading of the peeling arm during different stages in the test involves a plastic-plastic deformation, which agrees with the material behavior in laminates presented by Kinloch et al. The energy dissipated due to loading and unloading was derived in the ICPeel program. In this particular case, there is more dissipated energy involved in the peeling for the 90-degree experiment when it is compared to the 45-degree experiment. However, fracture energy for all peeling angles works in a range from 200 to 240 J/m², which affirms that the fracture energy does not depend on the test geometry (applied peel angle and thickness of the peel arm). The fracture energy depends on the material parameter (Young's modulus and yield strength) [33]. Hence, there is more energy involved in the process, but the fracture energy is almost the same for each peel angle orientation.

Table 7. Material properties used in the energy calculation

Input Values						Output Values			
E(GPa)	σ_y (Mpa)	h(mm)	b(mm)	Force(N)	θ (deg)	G_a (J/m ²)	G_{db} (J/m ²)	G (J/m ²)	Correction (%)
1.29	20.86	0.84	20	12.46	90	233.49	389.98	623.17	62.55
1.29	20.86	0.84	20	18.87	60	219.47	252.68	472.16	53.56
1.29	20.86	0.84	20	27.63	45	201.74	171.85	373.60	46.09

$$CFPD = \left(\frac{G_{db}}{G} \right) \times 100 \quad (20)$$

The correction factor for the plastic deformation (CFPD) was also verified for each angle configuration by using equation 20. These values relate the plastic work done in the bending of the peel arm (G_{db}) and the total input energy (G). Moore and Williams [35] mentions the

importance of these values because each correction for plastic deformation should not be too large. The author did not specify a range of values, but the values presented in this project works in a range between 47% and 65%. Possible factors, which can contribute with these values, can be related to the material properties or the peeling force obtained in the experiment. It was difficult to differentiate the elastic-plastic region in the stress-strain curve, and the uncontrollable amount of material in the peel arm after the peeling test provided different peeling forces. Different experiments were carried out to improve the correction for the plastic deformation, but all values are summarized in Table 7. Material properties used in the energy calculation are the most accurate values from all collected data. The results will be used in numerical analyses using COMSOL Multiphysics. In the simulation, an average fracture energy of 218.43 J/m² will be used in order to standardize the peeling process simulation because this energy does not depend on the angle orientation. Experimental and numerical results will be compared, and the effect in the correction for the plastic deformation will be discussed in the following sections.

5.5 Results in COMSOL

5.5.1 J-integral results

Figure 5.6 describes the von Mises equivalent stress distributions for the 90-degree peeling test. The Mo layer sustains much of the stress distributed in the whole model because a prescribed displacement was applied at the top edge of this layer. It also shows that the stress distribution around the crack, which is higher with respect to the rest of the specimen. The plot in Figure 5.7 shows the peel arm displacement as a function of the J-integral, using four contours around the crack labeled as T1, T2, T3 and T4. Each contour shows similar results, which confirms that the J-integral is path-independent. This plot estimated the critical separation value (δ_m) using the experimental energy release rate. The experimental fracture energy was determinate to 218.43 J/m² for 90-degree peeling test, and an interpolation using that energy in the 2-D simulation provides a value of 6.74 mm for the critical separation required to propagate the irreversible damage in the interface. Later, it will be explained that the estimated critical separation value (δ_m) of the J-integral is not same as the estimated the critical separation value (δ_m) of the cohesive zone model in section 5.5.2.

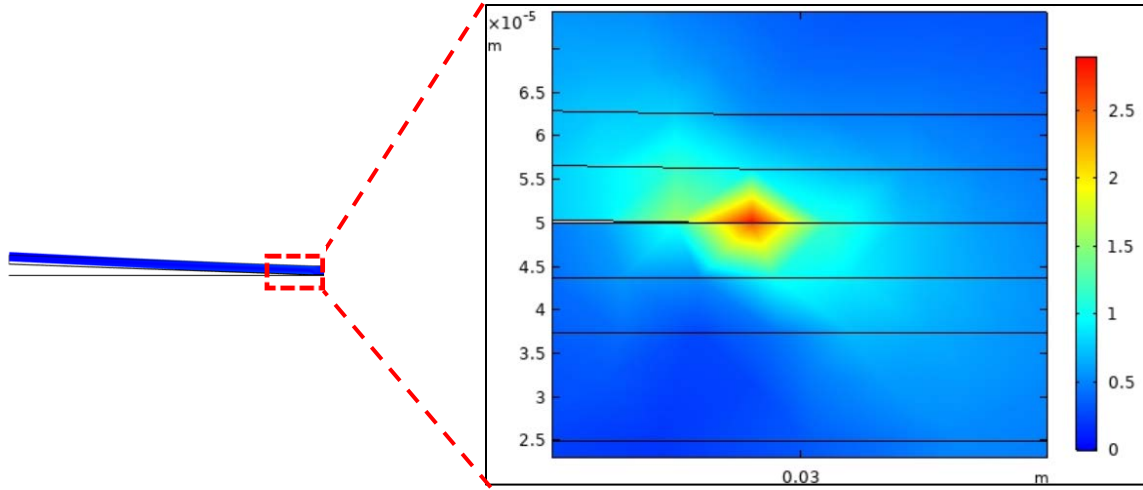


Figure 5.6. Normal stress distribution in X direction around the crack tip for 90-degree.

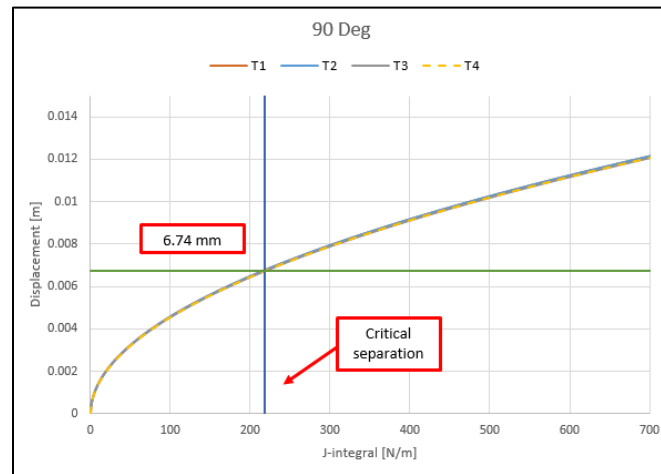


Figure 5.7. Displacement vs J-integral for 90-degree peeling test.

Figure 5.8 shows the calculated displacement versus the energy release rate for the 45 and 60 degrees using the same conditions as it was used in the 90-degree simulation. The energy was 218.43 J/m^2 with a critical separation of 0.79 mm (see Figure 5.8a) for the 45-degree peeling test, and 0.82 mm (see Figure 5.8b) for the 60-degree peeling test. These plots show that the critical separation is initiated faster when the angle is decreased. Simulations for 45 and 60 degrees were carried out to demonstrate the versatility of using COMSOL simulations, but the coming 3-D analysis using a finite element analysis is focused on the 90-degree peeling test. 2-D simulations

for 45 and 60 degrees were used to get more information about how fast the critical displacement is generated using different peel angle.

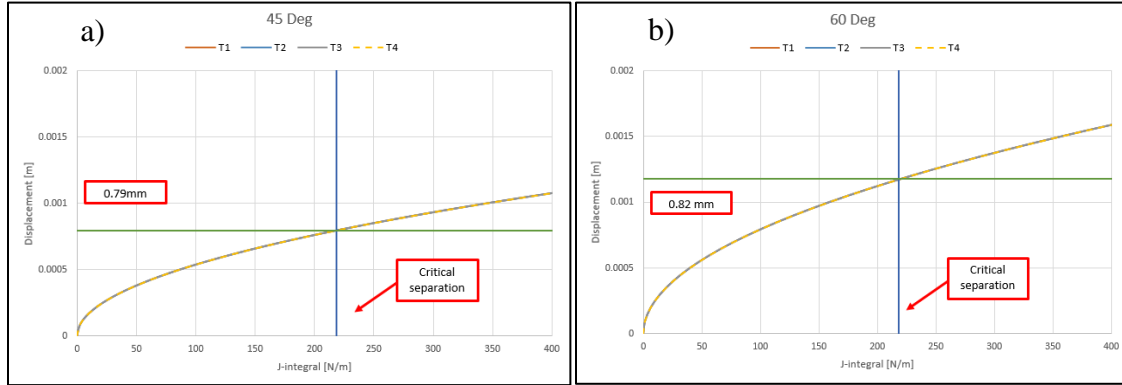


Figure 5.8. Displacement vs J-integral. (a) 45-degree test, (b) 60-degree peeling test.

5.5.2 Cohesive model results

Figure 5.9 shows the stress distribution in the sample for 90-degree using the geometry described in section 4.2.2. This shows that the highest equivalent stress is distributed broadly in the Mo layer (0.84 mm thickness). The Mo layer had a prescribed displacement applied at the top edge, which explains the high equivalent stress compared with the bottom layer (SS layer). This result agrees with the high stress concentration showed in the J-integral results, where the stress is located at the same region.

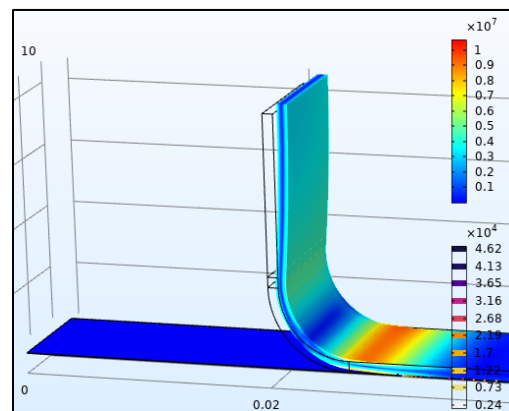


Figure 5.9. Equivalent stress (Pa) distributions for 90 degrees.

Figure 5.10 shows a progressive interfacial failure present in each simulation. The deboned region can be seen in red, while the healthy region is shown in green. The failure (red area) constantly increases due to the prescribed displacement. A total contact force tool in COMSOL software was included in the simulation in order to measure the maximum force achieved for the 90-degree test and the respective critical separation. The analysis in section 4.2.3 provides a penalty stiffness of $3.49 \times 10^9 \text{ N/m}^3$. The simulation did not have convergence issues, but the penalty stiffness importance was always considered in the analysis, as it was mentioned by Song et al. [66] in their simulation of progressive delamination. The plot in Figure 5.11 represents the force required to start the deboning process for 90-degree peeling test. At a load of approximately 9.69 N, the load stabilizes, which indicates the interfacial delamination between Mo and SS layers. In this simulation, two probes were included in the model to measure the displacement. One probe was located at the tip of the Mo layer and the other was located at the crack tip (Mo/SS interface). These two probes were used to measure a direct displacement during the delamination between layers. In Figure 5.11, the probe at the tip of the Mo layer was labeled as input displacement and the second probe was label as failure displacement. The delamination was set up to be at 0.5 mm , and the penalty stiffness of $3.49 \times 10^9 \text{ N/m}^3$ contributed with 28.58 % of the difference with the experimental peel force. The penalty stiffness was increased until it matches the experimental results. This was achieved when the penalty stiffness was increased from 3.49×10^9 to $11.866 \times 10^9 \text{ N/m}^3$. The plot in Figure 5.12 shows that the experimental and numerical results have a good agreement with each other. In this figure, the peel force stabilizes at 12.45 N, and it demonstrates that the peeling process for 90-degree could be replicated in COMSOL software with a small difference.

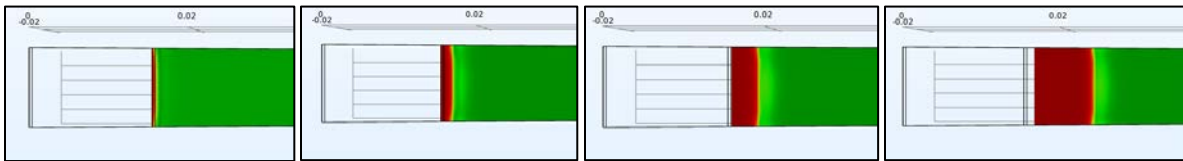


Figure 5.10. Progressive interface delamination.

Even though the correction for the plastic deformation presented in equation 20 had values between 47% and 65%, the good agreement between experimental and numerical results shows that it did not have a significant effect in the computation analysis. This was a concern in numerical

simulation because the protocols implemented in the experiment states that these values should be small to prevent errors in the determination of energy releases rate [35].

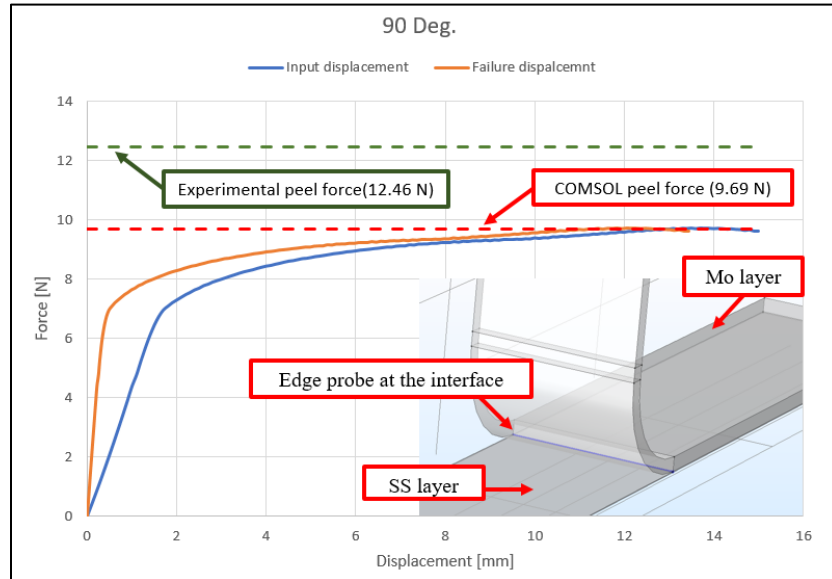


Figure 5.11. Experimental and numerical 90-degree peeling test.

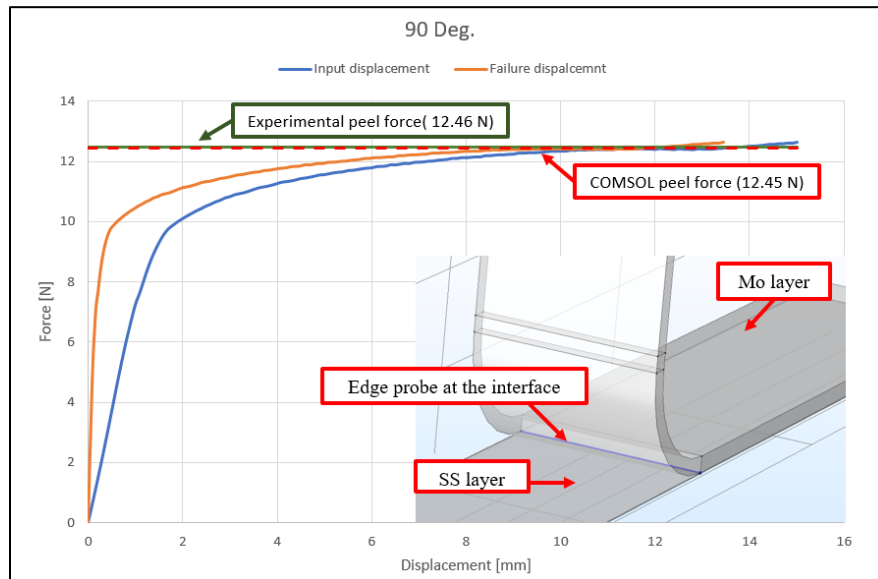


Figure 5.12. Improved results for the 90-degree peeling test.

Comparing the results using the 2-D and 3-D simulation in terms of critical separation, Figure 5.7 and Figure 5.12 show that the critical separation occurs faster in the cohesive model simulation than in the 2-D J-integral. The 2-D J-integral showed a critical separation located at 6.74 mm while the 3-D simulation showed a separation at 0.5 mm. A possible reason for the difference in critical separation may be the tool used in COMSOL to measure the separation displacement at the crack. The 2-D simulation has a progressive displacement increment in the top edge of the peel arm, which produce a critical displacement of 6.74 mm using an energy release rate of 218.43 J/m^2 . Figure 5.13 represents the progressive displacement increment in the 2-D simulation, and it shows how the stress increases. There is not a virtual crack propagation, but the energy and displacement constantly increase. On the other hand, the 3-D simulation provides a representation of the delamination as the displacement increases (see Figure 5.10).

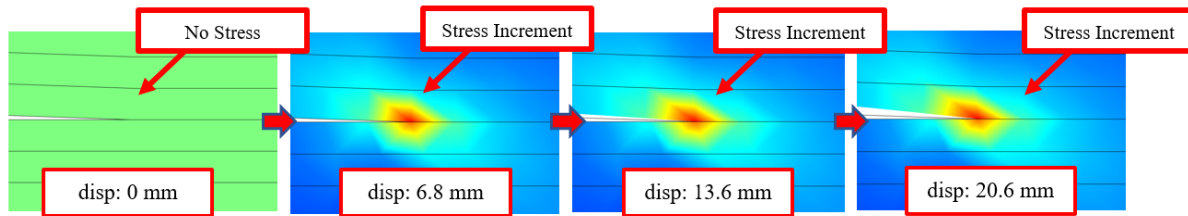


Figure 5.13. Progressive increment in energy.

More cohesive analyses using different orientation angles can be implemented in order to compare both experimental and numerical results, but it is beyond the scope of the present work. The experiments for 45 and 60 degrees were carried out to analyze the peel behavior using different orientation angles for a specific solar panel (Hanergy SP-08 flexible CIGS). 2-D simulations for 45 and 60 degrees were carried out to demonstrate the versatility that COMSOL provides to the user. Even though the experiment for 90-degree peeling test was simulated, this was successfully compared with the numerical simulation. The assumptions made for the traction –separation law were verified and they can be used to predict the delamination using the cohesive model.

6. CONCLUSION AND FUTURE WORK

6.1 Conclusion

A vast amount of literature is available on theoretical analyses of cohesive models and J-integrals in different structures and material compositions. In solar cells, the study is focused on the analysis of imperfections in the surface of the layers, but there is a lack of information about the interface analysis between layers. This reflects the importance of performing a complete analysis of the crack propagation, and the interest in predicting this type of failure.

In the peeling test, the force required to start the deboning process is taken as the average force for several measurements at different orientation angles. Peeling tests for 45 and 90 degrees showed greater scatter than the 60-degree test. The reason for this difference is unclear because the conditions used in each test were the same. The specimens were tested in the same MTS machine with similar dimensions and speed rate. The data collected showed random oscillation with different amplitudes and frequencies. If there is a random oscillation, each test was repeated, so the average peel force could be obtained for all angle settings.

The energy-balance proposed by Kinloch et al. [33] and the standards for measuring the fracture toughness of bonded laminates [35] have been implemented for the analysis. The results show that the energy release rate was independent of the peel angle. Peel angles of 45, 60 and 90 degrees show similar energy release rates. An energy releases rate of 218.43 J/m^2 was used in order to standardize the peeling process simulation. Dissipated energy was greater in the 90-degree experiment than in the 45 and 60 degrees experiments.

For the bilinear traction-separation law used in COMSOL, it was assumed that the critical separation (δ_m) was 0.5 mm and the initial separation (δ_c) was half of this value. These values were estimated based on the experimental results and observations in the COMSOL simulation. The experimental result for the 90-degree peeling test showed that the delamination occurs around 1mm. The observation in COMSOL (2-D simulation) showed that the crack tip displacement was half of the displacement measured at the tip of peeling arm. The numerical result using these two assumptions was compared with the experimental results showing similar peeling force. The results indicate that it is possible to simulate the peeling test for flexible solar cells.

The path integration independency around the crack tip, characteristic of the J-integral method, was verified by using the finite element analysis (FEA) in COMSOL. Four contours around the crack were included in the analysis for each angle setting (45, 60 and 90 degrees). The results verify the path independency, and they were used to analyze the effect of angle orientation in the peeling test process. The critical separation occurs fast as the angle orientation decreases.

6.2 Future work

The experimental part of the project could also be improved. A single type of solar panel was used, which has a protection cover made of flexible plastic. The flexible plastic had some irregularities on its surface made by the manufacturing company. These irregularities could contribute to the experimental scatter in measurements for material properties in the peel arm and peel forces. Many trials were conducted using the flexible plastic cover in order to obtain consistency in the results.

A two-dimensional simulation was generated for the J-integral calculations. A contour around the crack was created in order to compute the energy release rate as a function of the separation displacement for the Mo/SS interface. A 2-D model was created because there is only one possible contour around the crack. A three-dimensional (3-D) model implies that several contours around the crack must be created. These conditions create more complexity in the mesh generation, which makes the transition from 2-D to 3D more difficult to simulate. This implementation could be achieved if the contours and mesh are carefully created to prevent any convergence issue [68].

The 3-D COMSOL simulation could also be extended and improved. It would be of interest to develop a geometry for different orientation angles. This would allow us to get better comparisons with the available experimental data (45 and 60 degrees). The simulation in COMSOL was based on the 90-degree peeling test, but the change in angle orientation adds more complexity to the geometry and mesh generation. The peel arm of the geometry was bent 90-degree. For different angle orientations, the peel arm should always have a vertical position, which creates a curvature in the geometry. The numerical value of this curvature could be obtained, but the implementation of this value in the geometry using COMSOL was a complicated process to achieve. COMSOL does not have a proper user interface for creating geometries. Solidworks, for example, have specific tools, which makes it easy to design models and improve them. The

geometry in COMSOL was carefully created using vertices in specific coordinates. This process was time consuming with possibilities of making mistakes, which can affect the mesh generation. Discontinuities in the mesh was a major concern in the simulation because it can create convergence issues. Multiple faces were used for creating the mesh in the peel arm, and this process can become more complex if the geometry is not carefully created.

REFERENCES

- [1] Goetzberger, A., & Hoffmann, V. (2005). Photovoltaic solar energy generation. Springer, 112, (XII, 234)
- [2] Sabu, T., El Hadji, M. S., Nandakumar, K., Samuel, O. O., & Jihuai, W. (2019). Nanomaterials for solar cell applications, Elsevier.
- [3] Eslami Majd, A., & Nnamdi Ekere, N. (2020, August). Crack initiation and growth in PV module interconnection. Elsevier Inc., 206, 499-507, <https://doi.org/10.1016/j.solener.2020.06.036>.
- [4] Hwang, I., Jeong, Y., Shiratori, Y., Park, J., Miyajima, S., Yoon I., & Seo, K. (2020, November 18). Effective photon management of non-surface-textured flexible thin crystalline silicon solar cells. Cell Reports Physical Science, 1(11), 100242, <https://doi.org/10.1016/j.xcrp.2020.100242>.
- [5] Noufi R., & Zweibel, K. (2006, May 07). High-efficiency CdTe and CIGS thin-film solar cells: highlights and challenges, in IEEE 4th World Conference on Photovoltaic Energy Conference, Waikoloa.
- [6] Ramanujam, J., & Singh, U. (2017, April 20). Copper indium gallium selenide based solar cells – a review. Energy and Environmental Science, 10, 1306–1319, <https://doi.org/10.1039/c7ee00826k>.
- [7] Wilson, D. (2019, December 13). Wearable solar cell systems. Taylor & Francis Group, Engineering & Technology, 1, 164, <https://doi.org/10.1201/9780429399596>.
- [8] Polman, A., Knight, M., Garnett, E. C., Ehrler, B., & Sinke, W. C. (2016, April 15). Photovoltaic materials: present efficiencies and future challenges. Science, 352(6283), <https://doi.org/10.1126/science.aad4424>.
- [9] Mufti, N., Amrillah, T., Taufiq, A., Sunaryono, Aripriharta, Diantoro, Zulhadjri, M., & Nur, H. (2020, September 01). Review of CIGS-based solar cells manufacturing by structural engineering. Solar Energy, Elsevier, 207, 1146-1157, <https://doi.org/10.1016/j.solener.2020.07.065>.
- [10] Gilioli, E., Albonetti, C., Bissoli, F., Bronzoni, M., Ciccarelli, P., Rampino, S., & Verucchi, R. (2019, February 15). CIGS-Based flexible solar cells, Springer, 365-382, https://doi.org/10.1007/978-3-319-94358-9_17.

- [11] Ramanujam, J., Bishop, D. M., Todorov, T. K., Gunawan, O., Rath, J., Nekovei, R., Artegiani, E., & Romeo, A. (2020, May 01). Flexible CIGS, CdTe and a-Si:H based thin film solar cells: A review. *Progress in Materials Science*, 110, 100619, <https://doi.org/10.1016/j.pmatsci.2019.100619>.
- [12] Zhu, X.-K., & Joyce, J. A., (2012, May). Review of fracture toughness (G, K, J, CTOD, CTOA) testing and standardization. *Elsevier*, 85, 1-46, <https://doi.org/10.1016/j.engfracmech.2012.02.001>.
- [13] Irwin, G. (1958). Fracture, Elasticity and Plasticity. *Encyclopedia of Physics*, 3 / 6. Springer, Berlin, 558-590.
- [14] Inglis, C. (1913). Stresses in a plate due to the presence of cracks and sharp corners. *Trans. Institute of Naval Architects*, 219-241.
- [15] Griffith, A. (1921). The phenomena of rupture and flows in solids. *Philos. Trans*, 163-198.
- [16] Westergaard, H. M. (1939). Bearing pressures and cracks. Cambridge, Mass. A49–A53.
- [17] Perez, N. (2017). *Fracture Mechanics*, Springer, XIV4018
- [18] Anderson, T. (2005). *Fracture Mechanics: Fundamentals and Applications*, Taylor & Francis Group.
- [19] Hillerborg, A., Modeer, M., & Petersson, P.-E. (1976, November). Analysis of crack formation and crack growth in concrete by means of fracture mechanics and finite elements, *Elsevier*, 6(6), 773-781, [https://doi.org/10.1016/0008-8846\(76\)90007-7](https://doi.org/10.1016/0008-8846(76)90007-7).
- [20] Barenblatt, G. (1962). The mathematical theory of equilibrium cracks in brittle fracture, *Advance in Applied Mechanics*, 7, 55-129, [https://doi.org/10.1016/S0065-2156\(08\)70121-2](https://doi.org/10.1016/S0065-2156(08)70121-2).
- [21] Petersson, P.-E. (1981, December 4). Crack growth and development of fracture zones in plain concrete and similar materials, Doctor Thesis. Lund Institute of Technology. Report TVBM-1006.174+10pp.
- [22] Elices, M., Guinea, G., Gomez Sanchez, F.J., & Planas, J. (2002). The cohesive zone model: advantages, limitations and challenges. *Engineering Fracture Mechanics*, 69(2), 137-163, [https://doi.org/10.1016/S0013-7944\(01\)00083-2](https://doi.org/10.1016/S0013-7944(01)00083-2).
- [23] Planas, J., Guinea, G., & Elices, M. (1999, January). Size effect and inverse analysis in concrete fracture, *International Journal of Fracture* 95, 367, <https://doi.org/10.1023/A:1018681124551>.

- [24] Bazant, Z. (2002). Concrete fracture models: testing and practice, *Engineering Fracture Mechanics*, Elsevier, 69,165-205.
- [25] Carpinteri, A., & Ferro, G. (2003). Fracture assessment in concrete structures, *Comprehensive Structural Integrity*, Politecnico di Torino, Italy, 7, 501-528, <https://doi.org/10.1016/B0-08-043749-4/07121-4>.
- [26] Needleman, A. (1990). An analysis of tensile decohesion along an interface. *Journal of the Mechanics and Physics of Solids*, 38(3), 289-324, [https://doi.org/10.1016/0022-5096\(90\)90001-K](https://doi.org/10.1016/0022-5096(90)90001-K).
- [27] Tvergaard, V., & Hutchinson, J. (1992, August). The relation between crack growth resistance and fracture process parameters in elastic-plastic solids. *Journal of the Mechanics and Physics of Solids*, 40(6), 1377-1397, [https://doi.org/10.1016/0022-5096\(92\)90020-3](https://doi.org/10.1016/0022-5096(92)90020-3).
- [28] Tvergaard, V., & Hutchinson, J. (1994, March). Effect of T -stress on mode I crack growth resistance in a ductile solid, *International Journal of Solids and Structures*, 31(6), 823-833, [https://doi.org/10.1016/0020-7683\(94\)90080-9](https://doi.org/10.1016/0020-7683(94)90080-9).
- [29] Lin, G. (1998). Numerical investigation of crack growth behavior using a cohesive zone model". Thesis, Technische Univ. Hamburg-Harburg, Hamburg (Germany), 29(49).
- [30] Cornec, A., Lin, G., & Schwalbe, K.-H. (2013). Guidelines for applying cohesive models to the damage behaviour of engineering materials and structures. *SpringerBriefs in Applied Sciences and Technology*.
- [31] Rice, J. (1968). A path independent integral and the approximate analysis of strain concentration by notches and cracks, *Journal of Applied Mechanics*, 35, 379-386.
- [32] Nunez, D. (2003). J- integral computations for linear elastic fracture mechanics in h,p,k Mathematical and Computational Framework, B.S.(Aerospace Engineering), The University of Kansas, Lawrence, KS.
- [33] Kinloch, A., Lau, C., & Williams, J. (1994). The peeling of flexible laminates, *International Journal of Fracture*, 66, 45-70. <https://doi.org/10.1007/BF00012635>
- [34] Diehl, T. (2008, June). On using a penalty-based cohesive-zone finite element approach, Part II: Inelastic peeling of an epoxy-bonded aluminum strip, *International Journal of Adhesion & Adhesive*, 28(4-5), 256-265, <https://doi.org/10.1016/j.ijadhadh.2007.06.003>.

- [35] Moore, D.R., & Williams, J. G. (2010, November). A protocol for determination of the adhesive fracture toughness of flexible laminates by peel testing: fixed arm and t-peel methods, an ESIS Protocol, Imperial College of London.
- [36] Bdour, M., Dalala, Z., Al-Addous, M., Radaideh, A., & Al-SadZ, A. (2020, July 19). A comprehensive evaluation on types of microcracks, sustainability, 12(16), 6416, <https://doi.org/10.3390/su12166416>.
- [37] Rupnowski, P., & Sopori, B. (2009, March 03). Strength of silicon wafers: fracture mechanics approach, International Journal of Fracture, 155, 67-74.
- [38] Papargyri, L., Theristis, M., Kubicek, B., Krametz, T., Mayr, C., Papanastasiou, P., & Georghinou, G. E. (2020, January 01). Modelling and experimental investigations of microcracks in crystalline silicon photovoltaics: A review, Renewable Energy, 145, 2387-2408.
- [39] Corrado, M., Paggi, M., & Berardone, I. (2016, December). A global/local approach for the prediction of the electric response of cracked solar cells in photovoltaic modules under the action of mechanical loads, Engineering Fracture Mechanics, 168, 40–57, <https://doi.org/10.1016/j.engfracmech.2016.01.018>.
- [40] Wang, M., Zhao, L., Fourmeau, M., & Nelias, D. (2018). Crack plane deflection and shear wave effects in the dynamic fracture of silicon single crystal, Journal of the Mechanics and Physics of Solids, 122, 472-488, <https://doi.org/10.1016/j.jmps.2018.09.031>.
- [41] Köntges, M., Kunze, I., Kajari-Schröder, S., Breitenmoser, X., & Bjørneklett, B. (2011). The risk of power loss in crystalline silicon based photovoltaic modules due to micro-crack, Solar Energy Materials and Solar Cells, 95, 1131-1137, <https://doi.org/10.1016/j.solmat.2010.10.034>.
- [42] Sander, M., Dietrich, S., Pander, M., Schweizer, S., Ebert, M., & Bagdahn, J. (2011). Investigations on crack development and crack growth in embedded solar cells, Reliability of Photovoltaic Cells, Modules, Components and Systems IV, 8112, 70-79.
- [43] Gou, X., Li, X., Wang, S., Zhuang, H., Huang, X., & Jiang, L. (2018 February 18). The effect of microcrack length in silicon cells on the potential induced degradation behavior, International Journal of Photoenergy, 2018, 1110-662X.

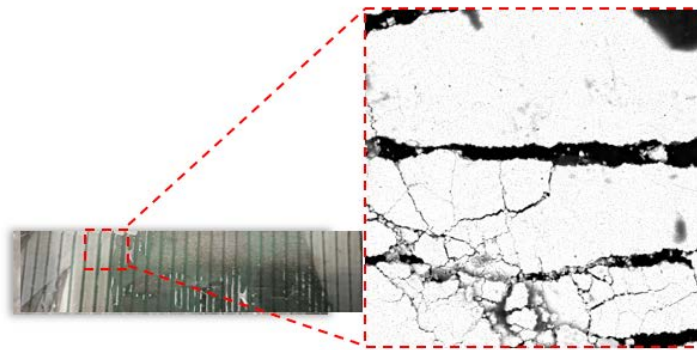
- [44] Wieghold, S., Morishige, A. E., Meyer, L., Buonassisi, T., & Sachs, E. M. (2017). Crack detection in crystalline silicon solar cells using dark-field imaging, *Energy Procedia*, 124, 526-531.
- [45] Jang, J., Sung, M., Han, S., & Yu, W-R. (2016). Prediction of delamination of steel-polymer composites using cohesive, *Composite Structures*, Elsevier, 160, 118-127, <https://doi.org/10.1016/j.compstruct.2016.10.025>.
- [46] Sun, C., & Jin, Z.-H. (2012). Chapter 9 - Cohesive zone model, *Fracture Mechanics*, Academic Press, 227-246.
- [47] Hanergy 8w cigs portable mobile solar phone charger sp-08 (2020, November 11). Retrieved from <https://www.newegg.com/p/2NZ-0025-00001>.
- [48] Li, X., Li, P., Wu, Z., Luo, D., Yu, H.-Y., & Lu, Z.-H.(2021, February). Review and perspective of materials for flexible solar cells, *Materials Reports: Energy*, 1(1), 100001.
- [49] Walter, T. (2015, January 01). Chapter Three - Reliability issues of cigs-based thin film solar cell, Elsevier, 92,111-150, <https://doi.org/10.1016/BS.SEMSEM.2015.05.001>.
- [50] Abou-Ras, D., Kistorz, G., Bremaud, D., Kälin, M., Kurdesau, F.V., Tiwari, A.N., & Döbeli, M.(2005). Formation and characterization of MoSe₂ for Cu(In,Ga)Se₂ based solar cells, *Thin Solid Films*,480-481, 433-438.
- [51] Kim, S.-T., Jeong, H-J., Kim, Y.-C., Bhatt, V., Kumar, M., Yun, J.-H., & Jang, J.-H. (2021, November). Effect of Na-doped Mo layer as a controllable sodium reservoir and diffusion barrier for flexible Cu(In,Ga)Se₂ solar cells, *Energy Reports*, 7, 2255-2261, <https://doi.org/10.1016/j.egyr.2021.04.040>.
- [52] Kam, H. O., Agileswari, R., Maniscalco, B., Arnou, P., Chandan Kumar, C., Bowers, J. W., & Bte Marsadek, M.(2018). Review on substrate and molybdenum back contact in CIGS thin film solar cell, *International Journal of Photoenergy*, <https://doi.org/10.1155/2018/9106269>.
- [53] Suryavanshi, P. S., Panchal, C.J., & Patel, A. L. (2021, January 01). Influence of thickness on physical and optoelectronic properties of DC sputtered bilayer molybdenum thin films for CIGS solar cell, *Materials Today: Proceedings*, 39(2021), 1884-1888.
- [54] Misra, P., Mandati, S., & Sarada, B. (2021, December 25). A non-vacuum dip coated SiO₂ interface layer for fabricating CIGS solar cells on stainless steel foil substrates, *Solar Energy*, 214, 471-477, <https://doi.org/10.1016/j.solener.2020.12.007>.

- [55] National Renewable Energy Laboratory. (2021, June 6). Retrieved from <https://www.nrel.gov/pv/copper-indium-gallium-diselenide-solar-cells.html>.
- [56] Morán, A., Nwakanma, O., Velumani, S., & Castaneda, H. (2020). Comparative study of optimized molybdenum back contact, *Journal of Materials Science: Materials in Electronics*, 31, 7524-7538, <https://doi.org/10.1007/s10854-020-03058-7>.
- [57] Lee, S.-J., Chen, Y.-H., Hu, S.-C., Lin, Y.-C., Chang, J.-W., Poon, T.-L & Ke, W.-C. (2013, May). Improved performance of amorphous Si thin-film solar cells on 430 stainless steel substrates by an electrochemical mechanical polishing process, *Journal of Alloys and Compounds*, 558, 95-98, <https://doi.org/10.1016/j.jallcom.2013.01.044>.
- [58] Liu, W.-S., Hu, H.-C., Pu, N.-W., & Liang, S.-C.(2014). Using a Ti/TiN composite structure as the diffusion barrier layer for CIGS solar cell application on stainless, 2014 21st International Workshop on Active-Matrix Flat panel Displays and Devices, IEEE, pp. 245–248. <https://doi.org/10.1109/AM-FPD.2014.6867182>.
- [59] Blösch, P., Pianezzi, F., Chirilă, A., Rossbach, P., Nishiwaki, S., Buecheler, S., & Tiwari, A. N. (2013, February). Diffusion barrier properties of molybdenum back contacts for Cu (In,Ga)Se₂ solar cells on stainless steel foils, *Journal of Applied Physics*, 113, 054506, <https://doi.org/10.1063/1.4789616>.
- [60] Kim, C.-W., Kim, H., Kim, J., & Jeong, C. (2016, May). Characterization of flexible CIGS thin film solar cells on stainless steel with intrinsic ZnO diffusion barriers, *Journal of Nanoscience and Nanotechnology*, 16, 5124-5127, <https://doi.org/10.1166/jnn.2016.12198>.
- [61] Brémaud, D. J. L. (2009). Investigation and development of CIGS solar cells on flexible substrates and with alternative electrical back contacts, Doctoral Thesis DISS, ETH Zurich 18194, 84, <https://doi.org/10.3929/ethz-a-005795511>.
- [62] Duplex Stainless Steel, (2020, October 10). Retrieved from <https://www.columbiametals.com/files/products/121.pdf>.
- [63] Lin, Y.-C., Peng, X.-Y., Wang, L.-C., Lin, Y.-L., Wu, C.-H., & Liang, S.-C. (2013, November 16). Residual stress in CIGS thin film solar cells on polyimide: simulation and experiments, *Journal of Materials Science*, 25, 461-465, <https://doi.org/10.1007/s10854-013-1610-7>.

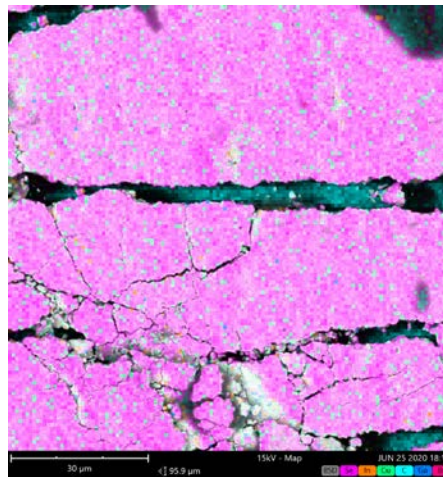
- [64] COMSOL Documentation. (1998-2020), Convergence using force or displacement control. Retrieved from <https://doc.comsol.com/5.6/docserver/#!/com.comsol.help.comsol/helpdesk/helpdesk.html>.
- [65] Tran, H. T. (2016). Experimental and computational study on fracture mechanics of multilayered structures, Graduate Theses and Dissertations, University of South Florida.
- [66] Song, K., Dávila, C. G., & Rose, C. A. (2013, August 24). Guidelines and parameter selection for the simulation of progressive delamination, NASA Langley Research Center Hampton, VA, United States, Conference paper.
- [67] Budynas, R. G., & Nisbett, J. K. (2015). Shigley's Mechanical Engineering Design. McGraw-Hill Education, 10th edition.
- [68] Bhushan, A., Panda, S. K., & Khan, D. (2015). Finite element evaluation of J-integral in 3D for nuclear grade graphite using COMSOL Multiphysics, COMSOL Conference in Pune.
- [69] Fors, F., & Mekanik, T. (2010, June). Analysis of metal to composite adhesive joints in space applications, Ph.D Thesis. Linköping University, Sweden, p. 115.

APPENDIX A. MATERIAL COMPOSITION FOR CIGS LAYER

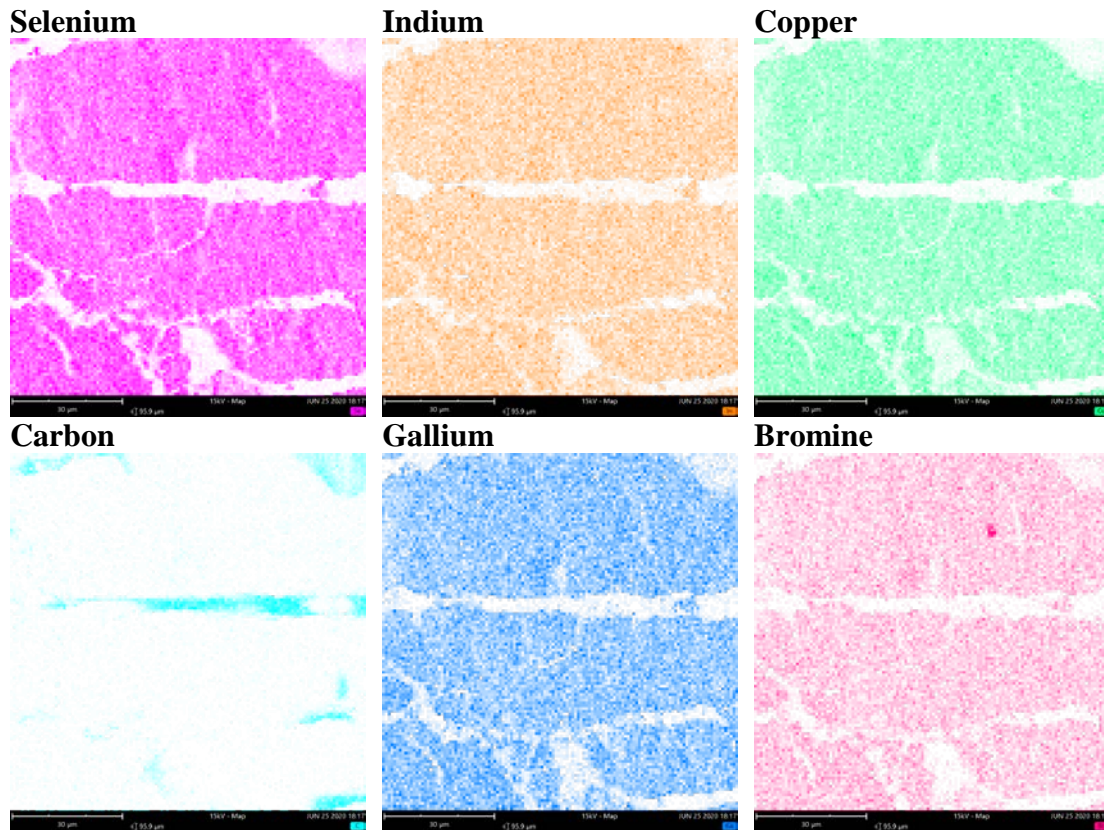
The following figures represent the material composition for the CIGS solar cell using the Phenom scanning electron microscope (SEM). Hanergy SP-08 flexible CIGS solar panel were used for all experiments. Rectangular samples were prepared with 100 mm length and 20 mm width. The figures represent the primary active layer (CIGS) showing micro cracks. It also shows different element such as selenium(S), indium (In) and copper (Cu), carbo(C), Gallium (Ga), Bromine (Br).



A.1. Hanergy SP-08 flexible CIGS solar sample under the SEM.



A.2. Material composition for the selected sample.

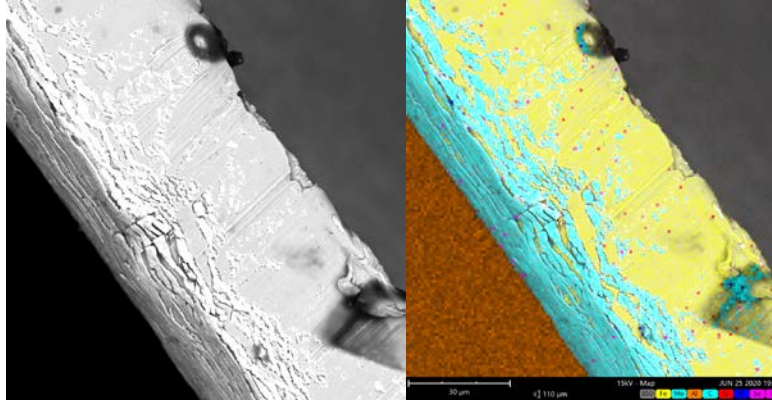


A.3. Material description for the sample tested in the experiment.

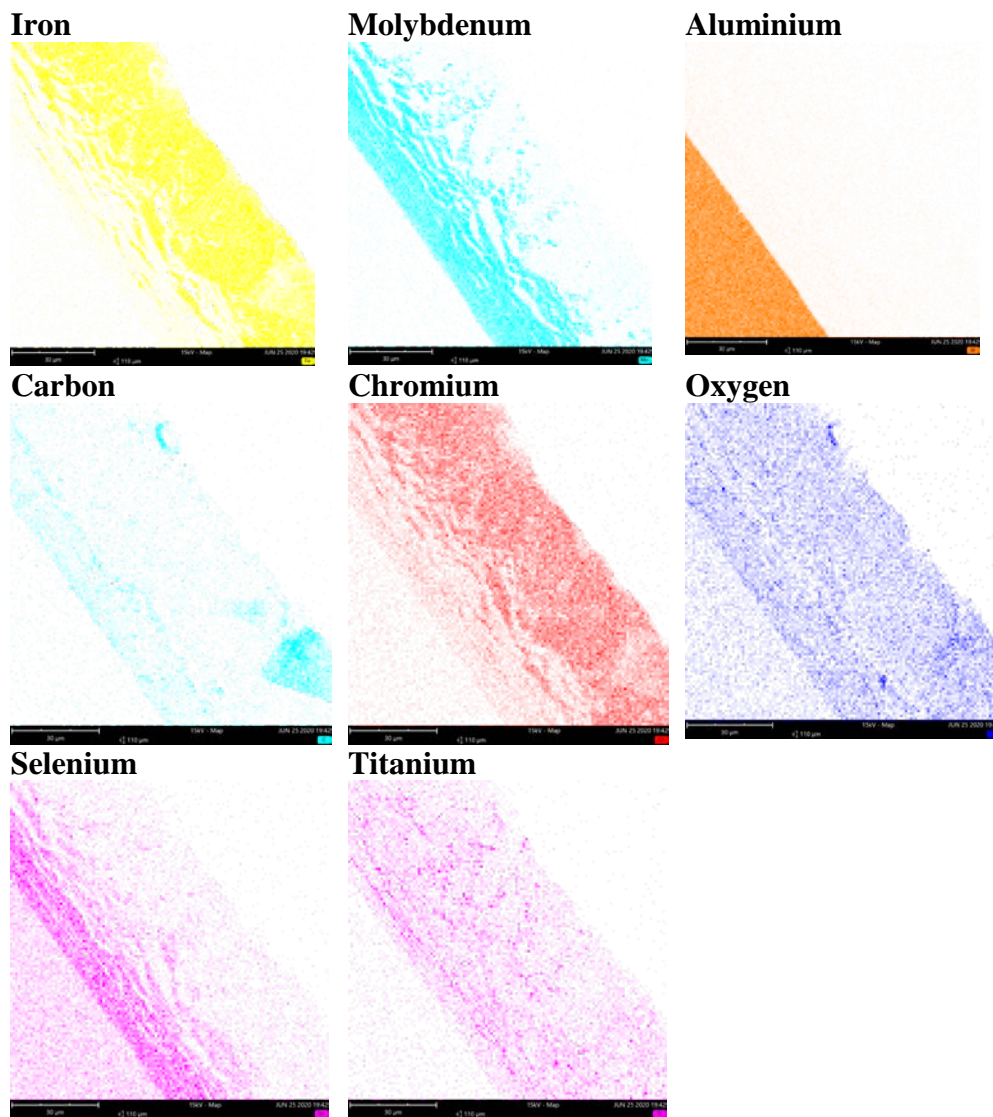
The following figure shows the Mo/SS interface using the scanning electron microscope (SEM). Different materials can be seen in this figure such as molybdenum iron (Fe), (Mo), aluminum (Al), Carbon(C), chromium (Cr), oxygen (O), selenium (Se) and titanium (Ti).



A.4. Sample under the SEM



A.5. SEM image of the Mo/SS sample



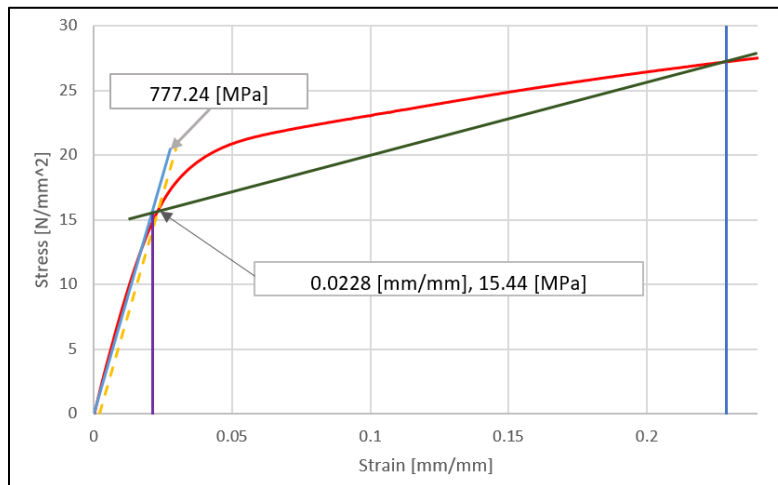
A.6. Cross section view of the CIGS sample with its material description.

APPENDIX B. PEEL ARM PROPERTIES

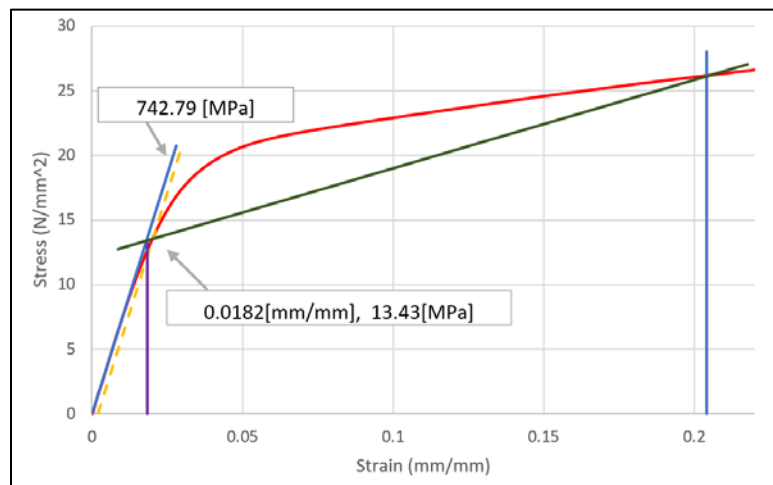
B.1. Without using a contact extensometer

The following figures represents the young's Modulus and yield strength for five different specimens without using an extensometer. The test was carried at 10 mm/min with a constant temperature of 24 °C. The tested samples had rectangular shapes of 100 mm length by 20 mm width. The results show values for yield strength in a range of 13 to 20 MPa, and a young modulus in a range of 700 to 1000 MPa.

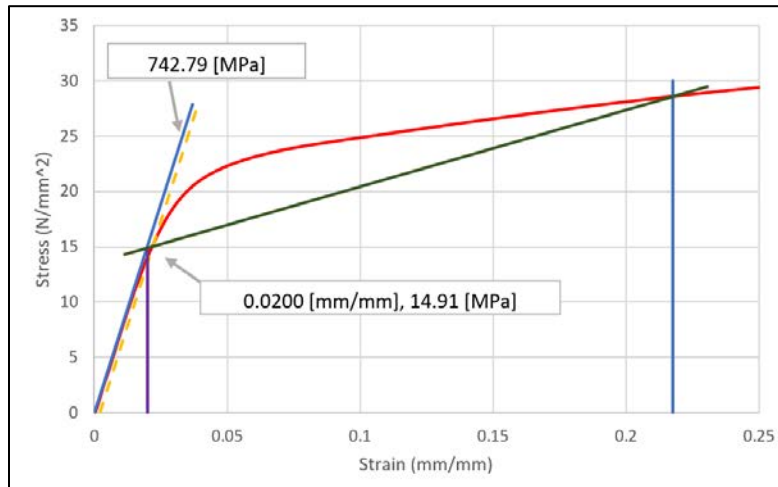
Test 1



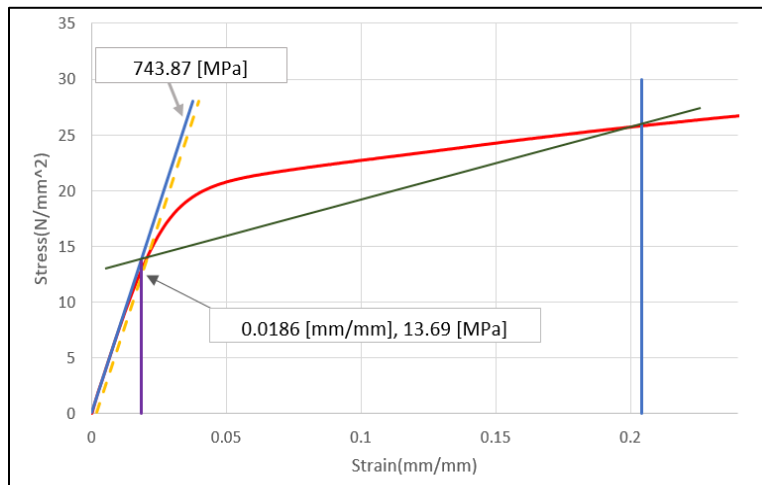
Test 2



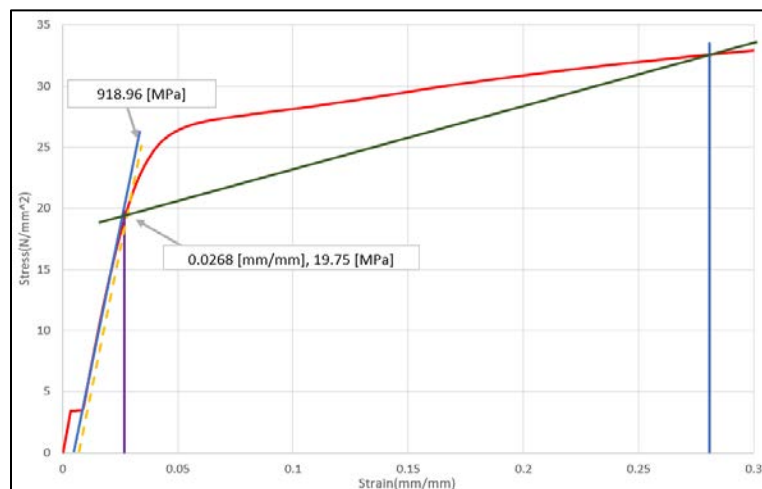
Test 3



Test 4



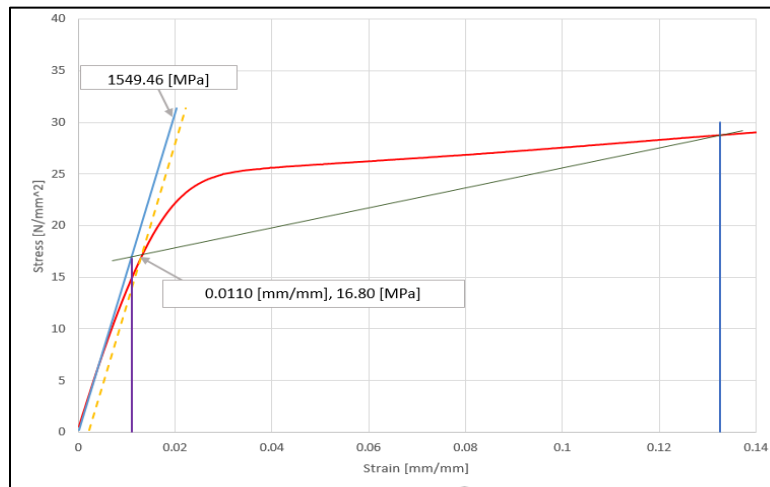
Test 5



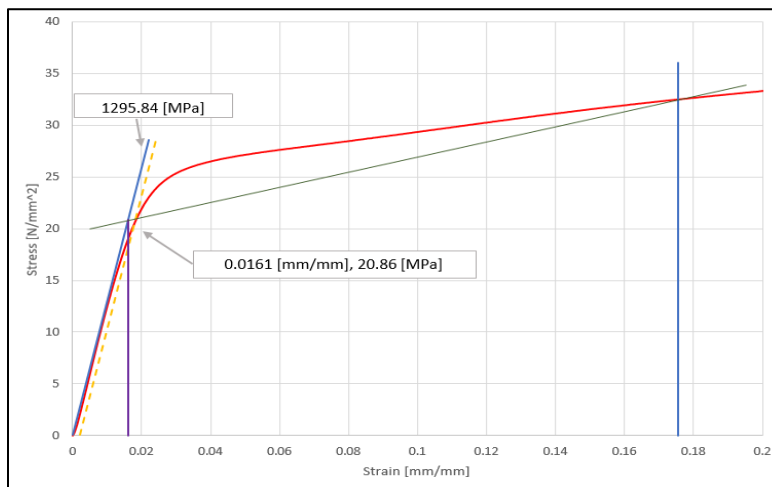
B.2. Using a contact extensometer

The following figures represents the young's modulus and yield strength for five different specimens using a contact extensometer. The test was carried at 10 mm/min with a constant temperature of 24 °C. The tested samples had rectangular shapes of 100 mm length by 20 mm width. The results show values for yield strength in a range of 13 to 21 MPa, and a young modulus in a range of 900 to 1600 MPa.

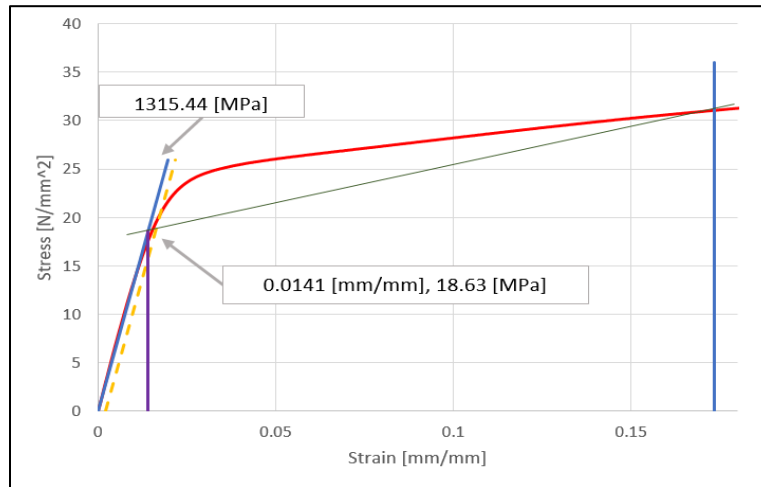
Test 1



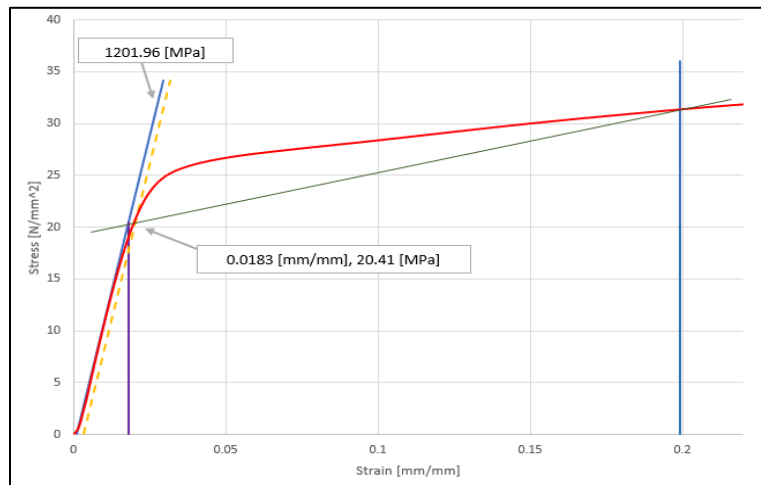
Test 2



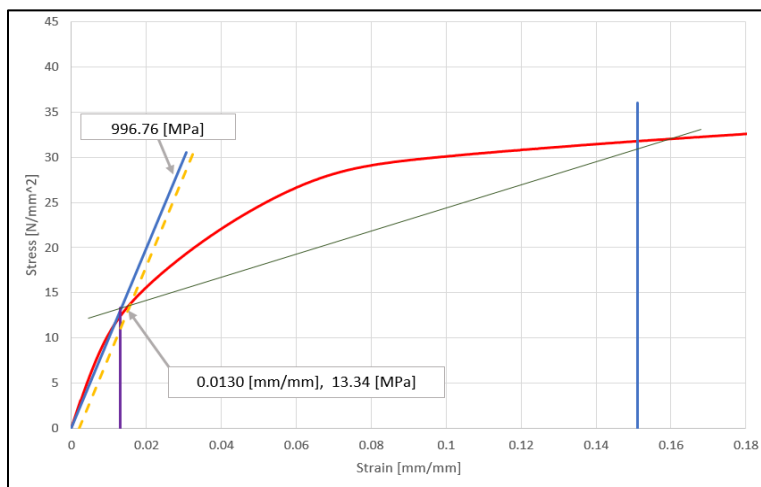
Test 3



Test 4



Test 5

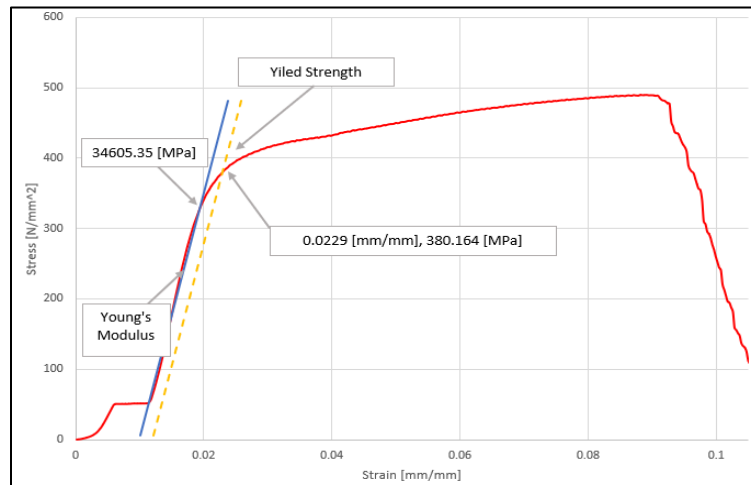


APPENDIX C. BOTTOM LAYER PROPERTIES

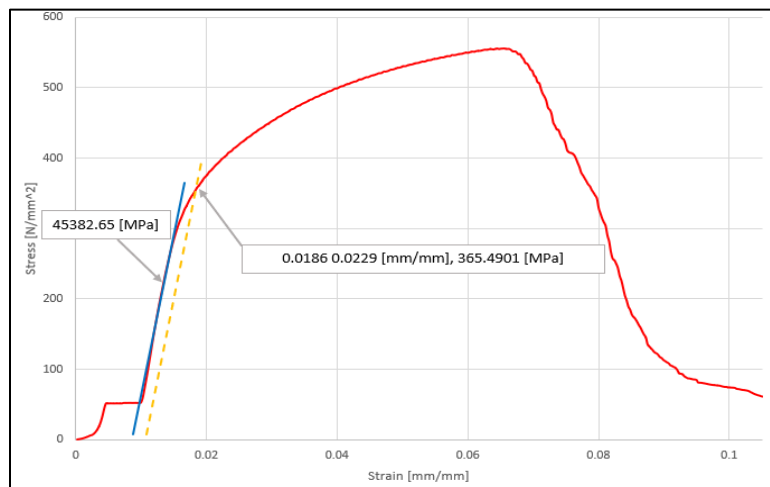
C.1. Without using a contact extensometer

The following figures represents the young's Modulus and yield strength for five different specimens without using an extensometer. The test was carried at 10 mm/min with a constant temperature of 24 °C. The tested samples had rectangular shapes of 100 mm length by 20 mm width. The results show values for yield strength in a range of 300 to 521 MPa, and a young modulus in a range of 35000 to 85000 MPa.

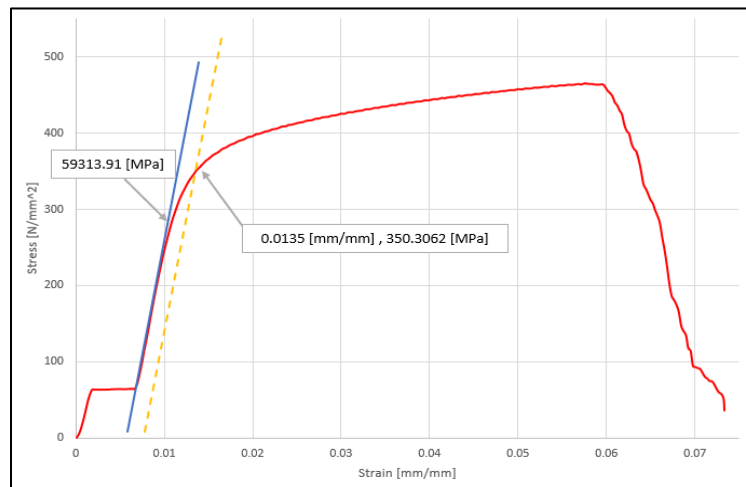
Test 1



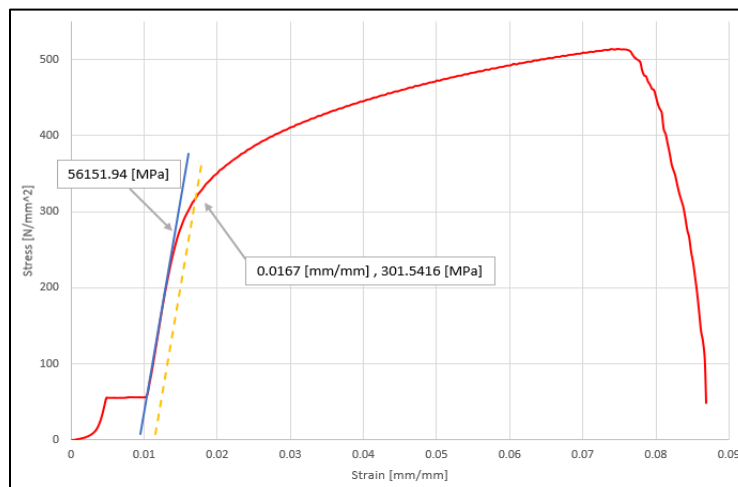
Test 2



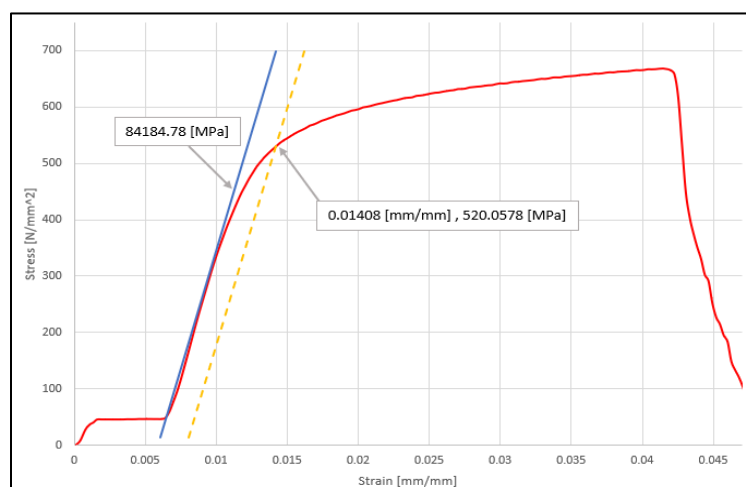
Test 3



Test 4



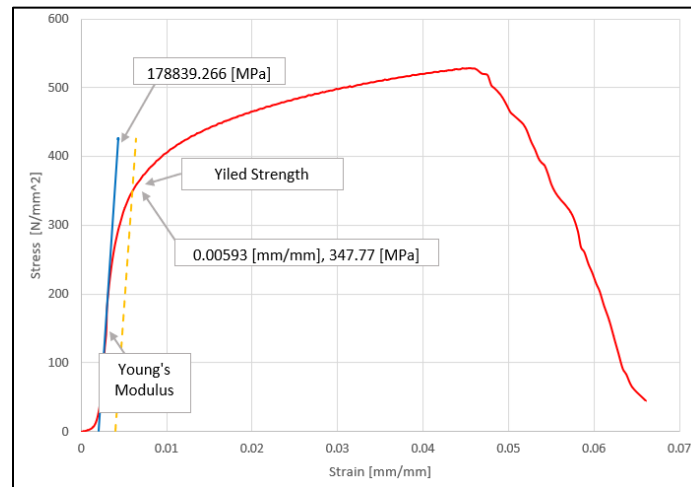
Test 5



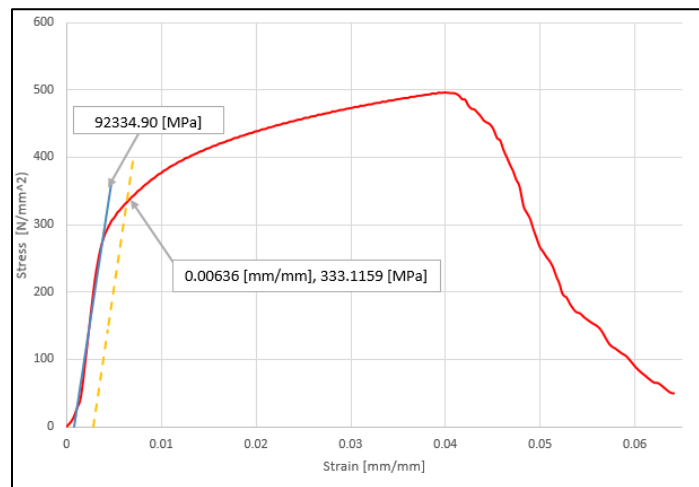
C.2. Using a contact extensometer

The following figures represents the young's Modulus and yield strength for five different specimens using a contact extensometer. The test was carried at 10 mm/min with a constant temperature of 24 °C. The tested samples had rectangular shapes of 100 mm length by 20 mm width. The results show values for yield strength in a range of 300 to 381 MPa, and a young modulus in a range of 39000 to 178 900 MPa.

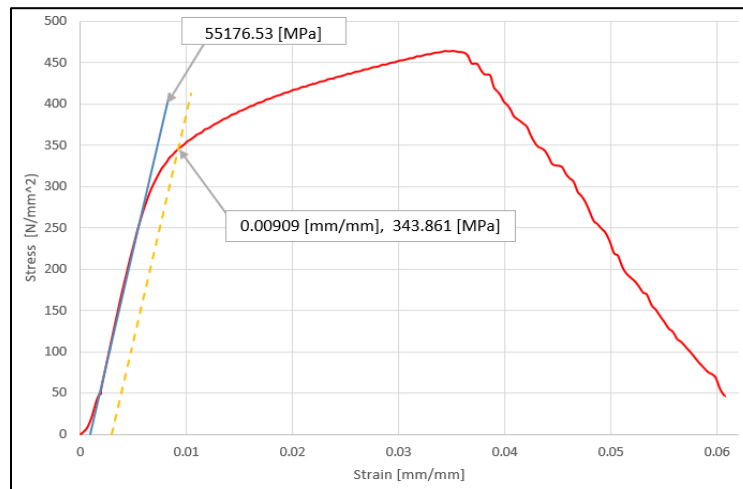
Test 1



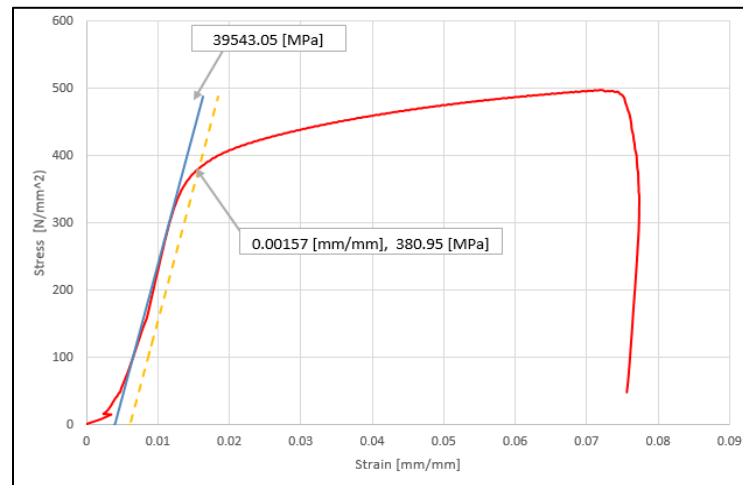
Test 2



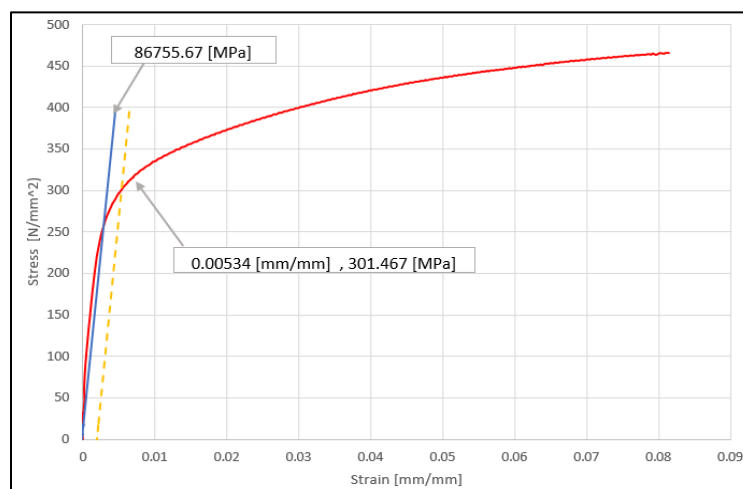
Test 3



Test 4



Test 5

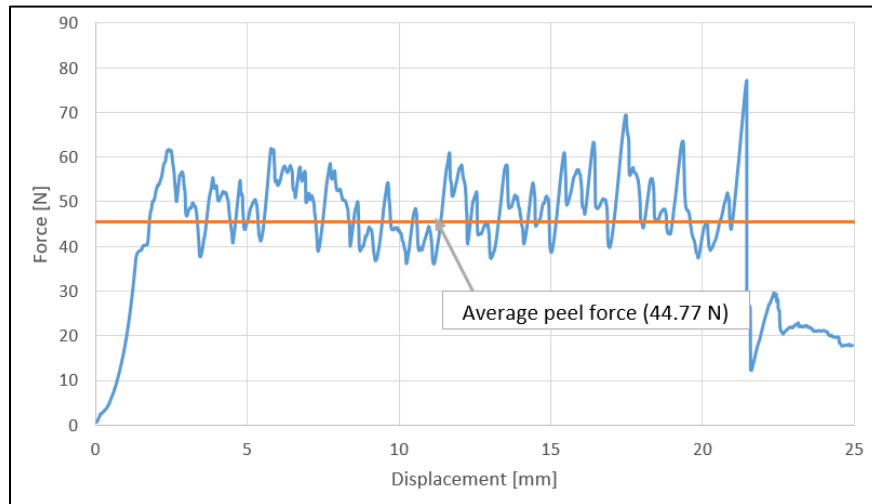


APPENDIX D. PEELING TEST RESULTS

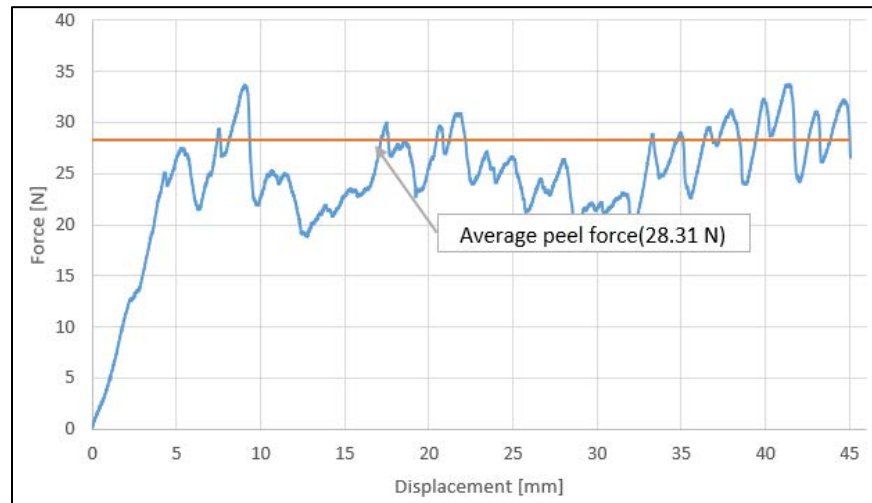
D.1. 45-degree peeling test

The following plots show the force-displacement curve for five different experiments using 45 degree peeling angle. The uniaxial tensile test was carried at 10 mm/min with a constant temperature of 24 °C. The tested samples had rectangular shapes of 100 mm length by 20 mm width. The force displayed in each force-displacement curve represents the peel force for the flexible protection and ZnO interface. Equation 21 was used to obtain the Mo and SS interface.

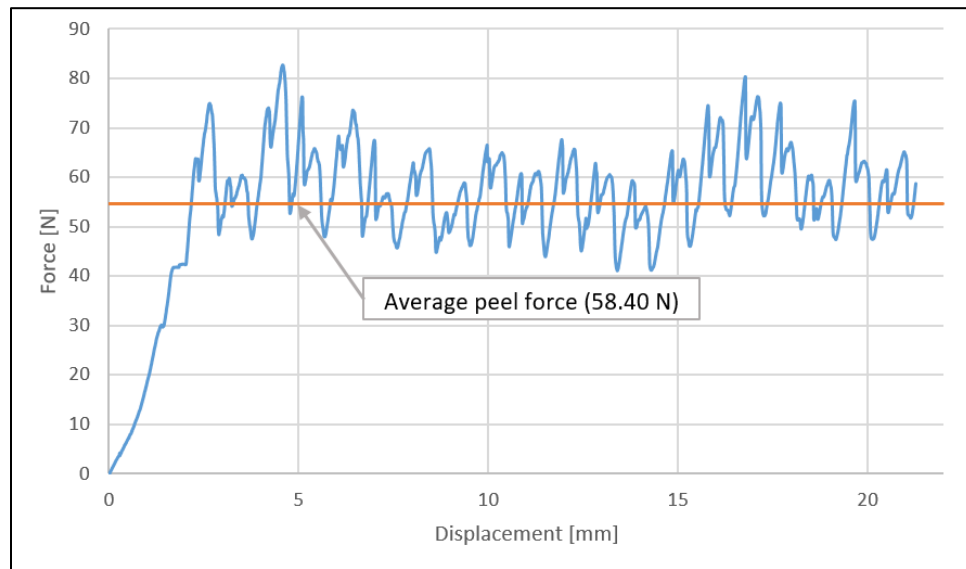
Test 1



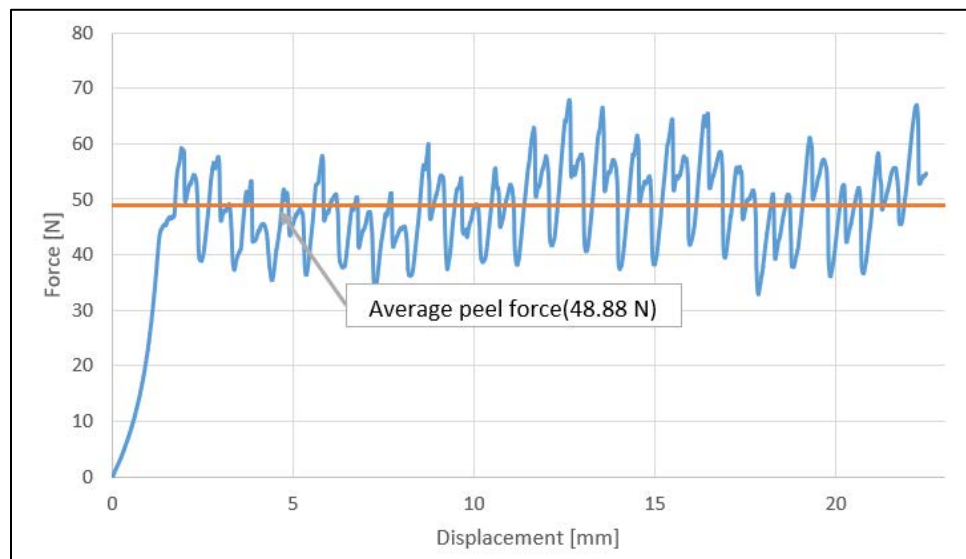
Test 2



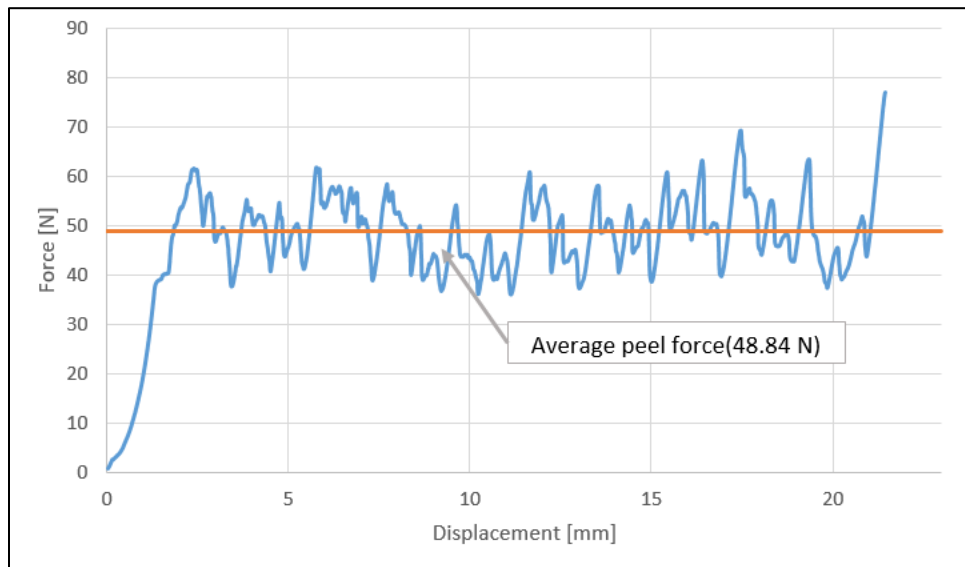
Test 3



Test 4



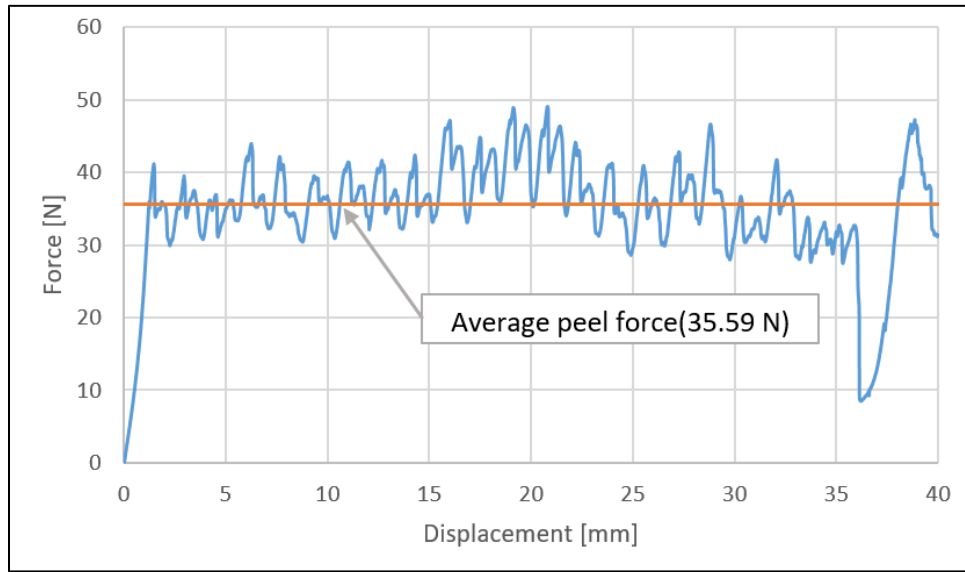
Test 5



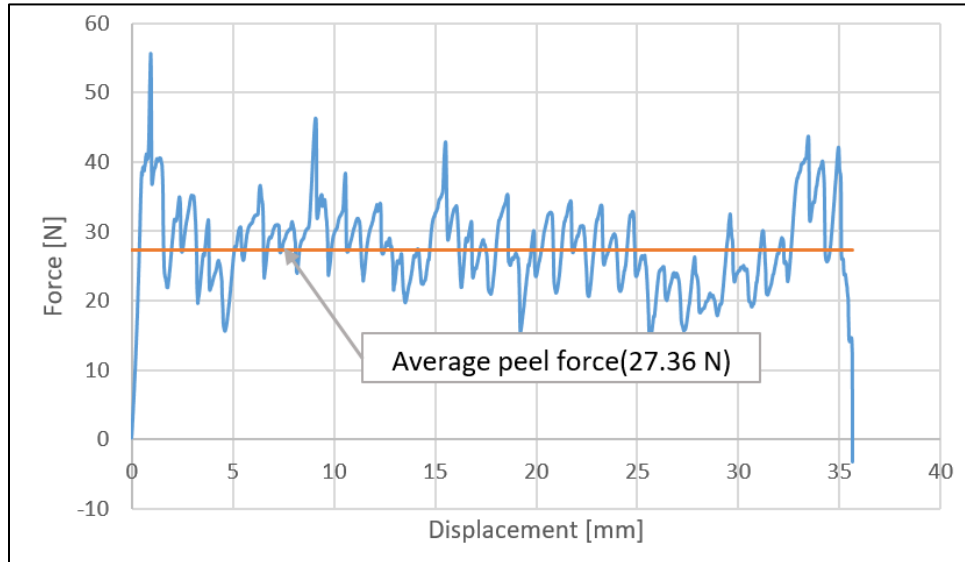
D.2. 60-degree peeling test

The following plots show the force-displacement curve for five different experiments using 60-degree peeling angle. The uniaxial tensile test was carried at 10 mm/min with a constant temperature of 24 °C. The tested samples had rectangular shapes of 100 mm length by 20 mm width. The force displayed in each force-displacement curve represents the peel force for the flexible protection and ZnO interface. Equation 21 was used to obtain the peeling force between the Mo and SS interface.

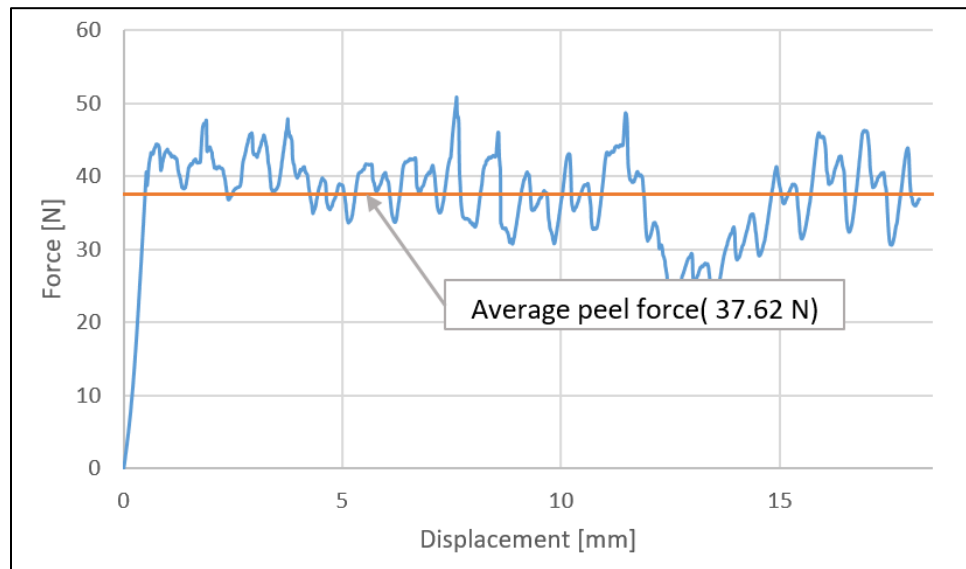
Test 1



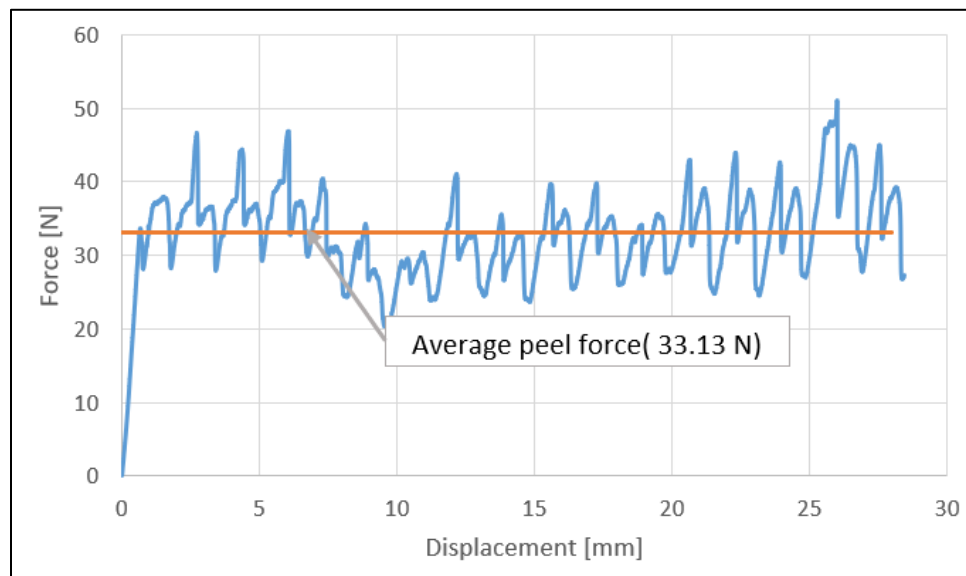
Test 2



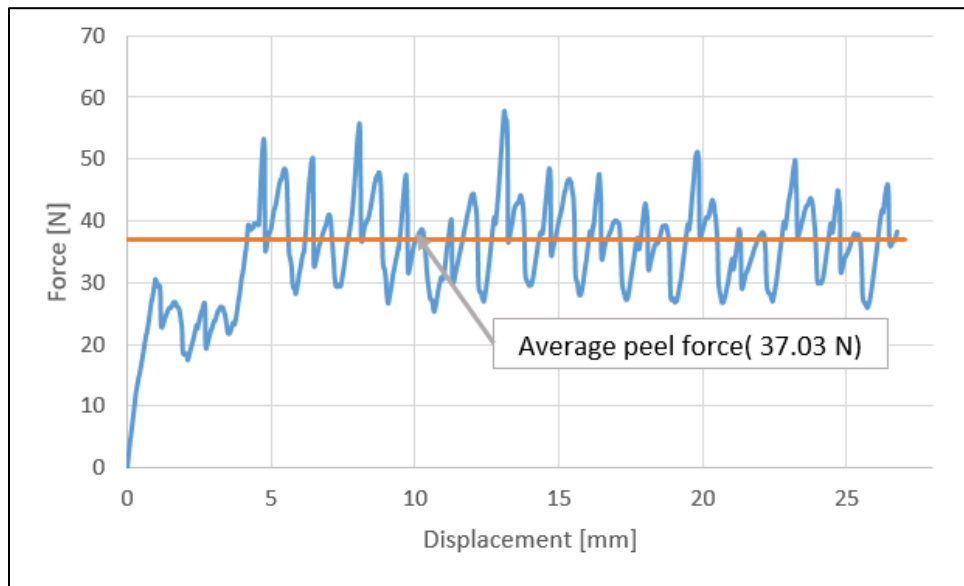
Test 3



Test 4



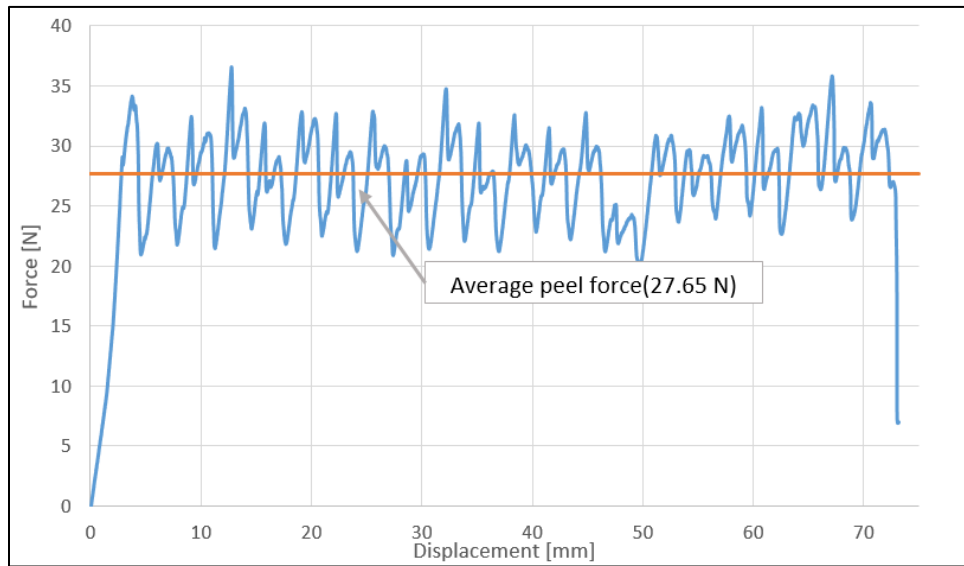
Test 5



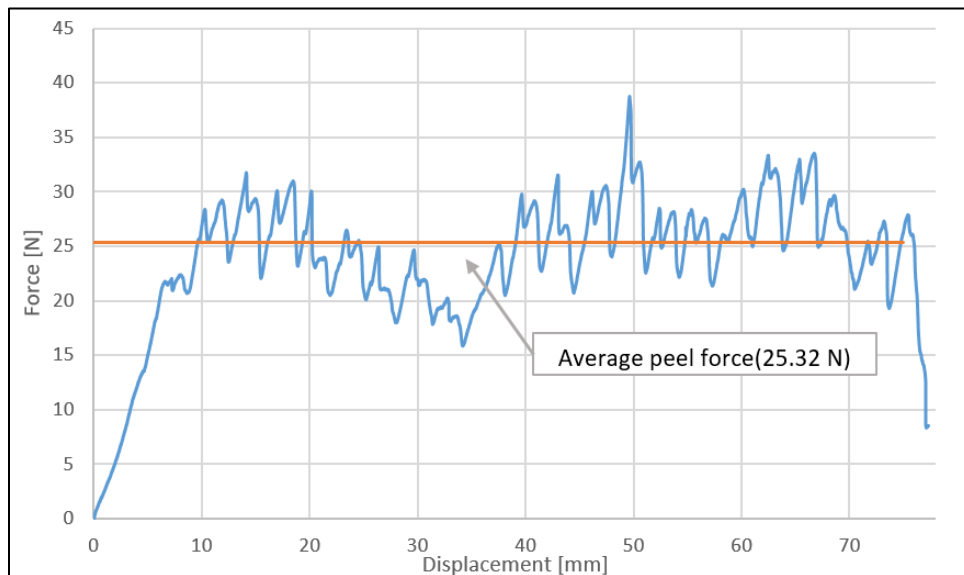
D.3. 90-degrees peeling test

The following plots show the force versus displacement for five different experiments using 90-degree peeling angle. The uniaxial tensile test was carried at 10 mm/min with a constant temperature of $24\text{ }^{\circ}\text{C}$. The tested samples had rectangular shapes of 100 mm length by 20 mm width. The force displayed in each force-displacement curve represents the peel force for the flexible protection and ZnO interface. Equation 21 was used to obtain the peeling force between the Mo and SS interface.

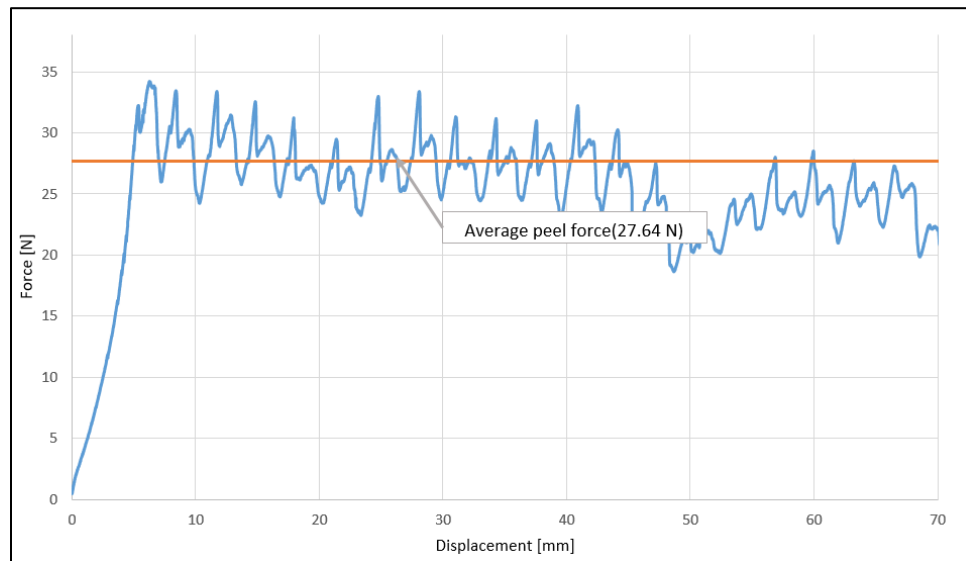
Test 1



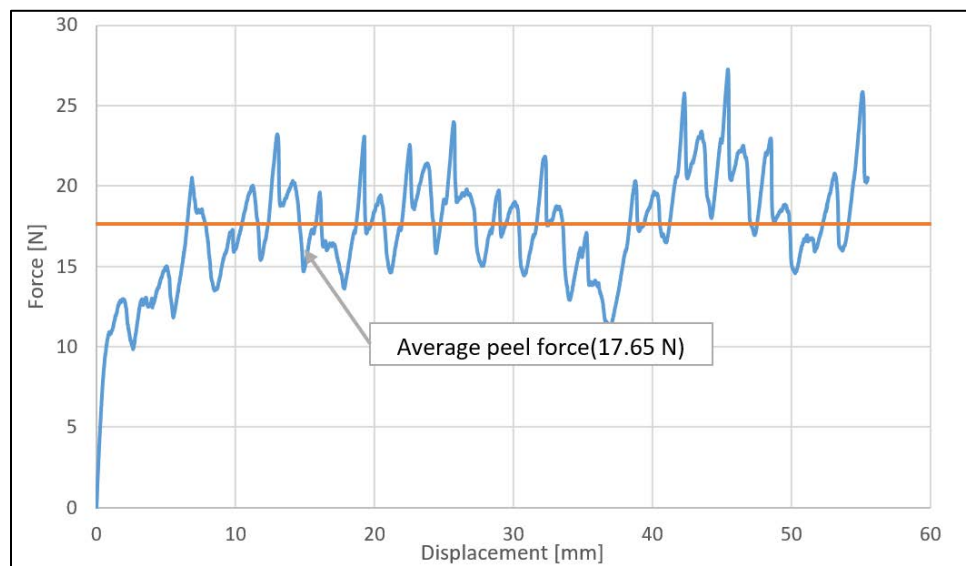
Test 2



Test 3



Test 4



Test 5

